EXPERIMENTAL INVESTIGATION INTO THE DYNAMICS OF THE AXISYMMETRIC MIXING LAYER UTILIZING THE PROPER ORTHOGONAL DECOMPOSITION

By JOSEPH H. CITRINITI

A dissertation submitted to the
Faculty of the Graduate School of the
State University of New York at Buffalo
in partial fulfillment of the requirements
for the degree of
Doctor of Philosophy
in Mechanical Engineering
February 1996

... To Jennifer and Gabriella

Acknowledgements

I would like to thank my advisor, Professor William K. George, for his help over the years and for not firing me like he suggested one stormy day last summer. I am glad we could pull it together. A special thanks goes to Mr. Scott Woodward whose work on this experiment (and just about every other one in the Mechanical and Aerospace Department) has earned him an honorary Ph.D...thanks Dr. Scott. I would like to thank my great friends in the department especially Dan Ewing for his help in trying to teach me mathematics. I am still not sure he succeeded (but the appendices are pretty impressive), Stu Cain for his friendship and his living room floor and Asad, Martin and Luciano. I hope that the next generation of the TRL lab finds it as stimulating an environment as we did.

This thesis could not have possibly been completed without the generous nature of both my family and my wife's. Thank you for always being there for us. The extra effort made by Ruth and Brian is greatly appreciated. Dad, to correct the ommission in my M.S. thesis here is your reference,

Citriniti, V.A., "The refraction of light and Snell's Law," Lecture at Sauquoit Valley Central School, December, 1984.

Finally, I would like to thank my wife for standing by me all these years and putting up with so much so that I could complete this degree. Thank you, I love you. And to our daughter, who pulled herself from the intensive care nursery to become the beautiful, intelligent little girl she is: someday, I hope, this thesis will make sense to you.

Abstract

Experimental data is presented from 138 channels of hot wire anemometry in a unique investigation of the large scale, or coherent, structures in a high Reynolds number ($Re_D = 80,000$) fully developed, turbulent axisymmetric shear layer. The dynamics of the structures are obtained from instantaneous realizations of the streamwise velocity field at a single plane, x/D = 3, downstream of the jet nozzle. The Proper Orthogonal Decomposition (POD) technique is applied to an ensemble of these realizations to determine optimal representations of the velocity field, in a mean square sense, in terms of an orthogonal basis. The coefficients of the orthogonal functions, which describe the temporal evolution of the POD eigenfunctions, are determined by projecting instantaneous realizations of the velocity field onto the orthogonal basis. The coherent structures are thus determined without having to resort to a dynamical systems model of the layer (v. Glauser et al. (1992)).

The coherent structure dynamics are visualized by examining the time history of the velocity field produced from the POD eigenfunction-coefficient (or PEA) expansion. Partial reconstructions of the velocity field using only the first PEA are presented to visualize the large scale structures in the mixing layer. Combining a time history of these reconstructions produces an animation of the large scale structures in the flow. It is possible to confirm that a model describing the interactions of the large scale structures in the mixing layer from Glauser et al. (1995) is consistent with the measurements using these animations.

Contents

A	ckno	wledgements	ii	
A	old Abstract			
Ta	Cable of Contents			
Li	st of	Figures	vii	
Li	st of	Tables	x	
1	Introduction			
2	\mathbf{Pro}	per Orthogonal Decomposition	6	
	2.1	Introduction	6	
	2.2	General Decomposition	7	
		2.2.1 This Application	9	
	2.3	Statistically Stationary Directions	10	
	2.4	Axisymmetric Mixing Layer	12	
		2.4.1 This Application	16	
3	Exp	perimental Design	18	

	3.1	Introd	luction	18
	3.2	Nume	rical Approximation	18
	3.3	Design	n Considerations	20
		3.3.1	Flow Field - Azimuthal Direction	21
		3.3.2	Design Implications	23
		3.3.3	Flow Field - Radial Direction	24
	3.4	Probe	Array Design	24
		3.4.1	Flow Blockage	25
		3.4.2	Transducer Design	25
		3.4.3	Aliasing Example in the Mixing Layer	31
4	Ane	emome	eter Probe Design	33
	4.1	Introd	luction	33
	4.2	Long 1	Hot Wire Probes	33
	4.3	The H	lot Wire as a Spatial Filter	34
	4.4	Exper	iment	36
		4.4.1	Flow field	37
		4.4.2	Experimental hardware	37
		4.4.3	Results of experiment	39
	4.5	Nume	rical solution	40
		4.5.1	Numerical solution method	44
		4.5.2	Numerical solution results	44
		4.5.3	Three-dimensional spectrum	45
	4.6	Applic	cation to this Experiment	53
		4.6.1	Heat Transfer Considerations	5.5

5	$\mathbf{E}\mathbf{x}\mathbf{p}$	erime	nt		59
	5.1	Introd	uction		59
	5.2	Facilit	y	•	59
	5.3	Instru	mentation		61
		5.3.1	Sampling overview		63
		5.3.2	Calibration		66
	5.4	Anemo	ometry	•	68
		5.4.1	Feedback loop		70
		5.4.2	Output stage		72
		5.4.3	Construction and assembly		75
		5.4.4	Anemometer Board Housing		82
		5.4.5	Operation		83
		5.4.6	Circuit performance		85
		5.4.7	Circuit noise properties		88
		5.4.8	Multiple channel testing		91
	5.5	Summ	ary		91
6	Pre	limina	ry Results		92
	6.1	Introd	uction		92
	6.2	Numer	rical Implementation		93
	6.3	Prelim	ninary Results		96
		6.3.1	Flow Field		96
		6.3.2	POD Decomposition	•	102
7	Res	ults			110
	7 1	Introd	uction		110

	7.2	POD Velocity Reconstruction	111
	7.3	Numerical Implementation	111
	7.4	Energy Distribution in Mixing Layer	112
	7.5	Temporal Resolution of Spatial Structures	121
		7.5.1 Animation	122
	7.6	Structure in the Axisymmetric Mixing Layer	123
		7.6.1 Single Azimuthal Mode Representation	130
	7.7	Four Azimuthal Mode Representation	133
8	Con	aclusions	138
	8.1	Turbulent Production Mechanism	138
	8.2	Recommendation for Further Study	140
Bi	ibliog	graphy	141
\mathbf{A}	Ker	nel Formulation	145
	A.1	Spectral analysis	146
	A.2	POD kernel Formulation	148
В	Ort	hogonal Eigenfunction Proof	150

List of Figures

1.1	Models for the evolution of large scale structure in the axisymmetric	
	mixing layer	4
2.1	Schematic of the jet mixing layer	13
3.1	Azimuthal mode number decomposition of the streamwise velocity cor-	
	relation	22
3.2	Probe array showing location of 138 probes	26
3.3	Aliasing example	28
3.4	Modal decomposition in the jet mixing layer: 30 points	29
3.5	Modal decomposition in the jet mixing layer: 48 points	30
4.1	Hot wire anemometer probe	35
4.2	Probe alignment in 4 wire experiment	38
4.3	Spectra in 4 wire experiment	41
4.4	Spectrum function, $E(k)$, of Helland et al. (1977) with Reynolds num-	
	ber dependence	43
4.5	Normalized, one dimensional spectra. log-log plot	46
4.6	Normalized, one dimensional spectra. log-linear plot	47
4.7	3-D spectrum for fixed wire length, $F_{11}(k_2)$	49

4.8	3-D spectrum for fixed wire length, $F_{11}(k_1)$	51
4.9	Filtering in 3-D spectrum for varying wire length	52
4.10	Azimuthal mode number filtering	56
5.1	Experimental jet facility	60
5.2	Hot wire probe mold	62
5.3	Spectrum from the mixing layer of the axisymmetric jet at $Re_D=80,000$	65
5.4	Sample calibration	69
5.5	Anemometer circuit diagram	71
5.6	Picture of 16 channel anemometer board	76
5.7	Photo plot of board layer 1	77
5.8	Photo plot of board layer 2	78
5.9	Picture of an emometer board housing	79
5.10	Circuit diagram of digital control board	80
5.11	Timing diagram for digital control board and A/D	81
5.12	Sketch of Wheatstone bridge	84
5.13	Spectra in mixing layer of jet using the Buffalo and Dantec anemometers	86
5.14	Coherence in mixing layer of jet using the Buffalo anemometer	89
6.1	Mean contours in the axisymmetric mixing layer	97
6.2	Mean and rms values of the streamwise velocity along a line in the	
	mixing layer	98
6.3	Spectral makeup of mixing layer	.00
6.4	Effect of spectral filtering	.01
6.5	Spectra in mixing layer; r/D=0.15, 0.28	.03
6.6	Spectra in mixing layer; r/D=0.41, 0.54	04

6.7	Spectra in mixing layer; $r/D=0.67$, 0.80	105
6.8	POD reconstruction of spectrum	107
6.9	POD reconstruction of instantaneous velocity	109
7.1	Energy distribution in the POD eigenvalues	113
7.2	Eigenspectra for azimuthal modes 0 and 1	116
7.3	Eigenspectra for azimuthal modes 2 and 3	117
7.4	Eigenspectra for azimuthal modes 4 and 5	118
7.5	Eigenspectra for azimuthal modes 6 and 7	119
7.6	Eigenspectra for azimuthal modes 8 and 9	120
7.7	Color contour plot of velocity field - Original velocity	125
7.8	Color contour plot of velocity field - Pea Reconstruction	126
7.9	Color contour plot of velocity field - Original Velocity	127
7.10	Color contour plot of velocity field - PEA reconstruction	128
7.11	Color contour plot of velocity field - PEA reconstruction	129
7.12	Color contour plot of velocity field - PEA Reconstruction	131
7.13	Color contour plot of velocity field - PEA Reconstruction	132
7.14	Color contour plot of velocity field - PEA reconstruction, no mean	134
7.15	Color contour plot of velocity field - PEA reconstruction, no mean	135
7.16	Color contour plot of velocity field - PEA reconstruction, no mean	136

List of Tables

6.1	Portion of area under spectra contained in the POD modes	108
7 1	Kinetic energy distributed in azimuthal modes for each POD mode	115

Chapter 1

Introduction

Large scale structures in turbulent flows have been known to exist for a number of years but their contribution to the dynamics of turbulent motion has only recently been investigated. In order to assess the influence of these structures on the turbulent field it is first necessary to identify them unambiguously. In 1967 Lumley proposed a method by which the most energetic structures of a turbulent flow field could be objectively recovered. The method he introduced to the turbulence community was based on the claim that the large scale, or coherent, structure occurs in an identifiable manner in a given ensemble of random vector fields, and this structure, or structures, contribute significantly to the total kinetic energy in the flow field. One turbulent field in which the Proper Orthogonal Decomposition, or POD, has been applied is the axisymmetric jet.

The integral eigenvalue equation resulting from the application of the POD to the instantaneous velocity vector in the axisymmetric jet mixing layer, was solved in an experimental investigation by Glauser (1987). The most energetic structure recovered by the POD in this decomposition contained 40% of the turbulent kinetic energy in

the flow. The second and third structures combined to contribute another 40% to the energy with the second containing a larger portion. Since the large scale structures in the flow were now known, it was possible to formulate a model describing the evolution of turbulent structures in the axisymmetric mixing layer. The model, from Glauser (1987), suggests that the mechanism for turbulence production in the mixing layer is based on two interacting rings shed from the jet nozzle a short time apart. Through induced velocity fields, the trailing ring is able to slow the convection of the first which causes the trailing ring to "leapfrog" through the larger outer ring (v. fig. 1.1). The outside ring, driven unstable by the trailing inner ring, forms an unstable, multilobed structure. Eventually, the outer ring breaks into small vortex rings which in turn are broken into smaller and smaller scales. The instability of the outer ring is driven by the stretching due to the induced velocity field from the following, inner ring.

In another description of the axisymmetric mixing layer, Hussain (1986) presented a model of the dynamics of the large scale structures in the layer. This model suggests that the turbulence production mechanism in the axisymmtric mixing layer is initiated by a cut-and-connect process. In this process, a single vortex ring is shed from the jet nozzle, grows as it is convected with the flow, and becomes unstable. At this point, the single, multi-lobed vortex cuts and reconnects to form a circular, center ring and many outer rings (v. fig. 1.1).

While both models appeared consistent with the measurements, they could not both be describing the same process because of the differences in the center of the shear layer at the high speed side and the modal formation at the low speed side. What was needed was a full field, simultaneous measurement of the instantaneous velocity so that the temporal dynamics of the large scale structures in the mixing

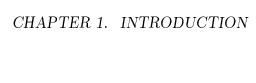


Figure 1.1: Two models for the motion of structures in the axisymmetric mixing layer. Part (a) from Glauser *et al.* (1995) and Glauser (1987) and (b) from Hussain (1986)

layer could be be visualized at all radial and azimuthal positions simultaneously.

Since the POD provides an objective technique by which energetic structures in a turbulent velocity field can be objectively recovered, it can be utilized to investigate the dynamics of structures in turbulent velocity fields, and specificly the axisymmetric mixing layer. To perform the POD in this case, it is necessary to determine the coefficients of the orthogonal expansion. These coefficients describe the temporal evolution of the structures and are vital to understanding the interactions in the mixing layer (George, 1988). The integral equation which must be solved to obtain these coefficients is not trivial because the velocity field downstream of the jet exit must be measured at all radial and azimuthal positions simultaneously. Since it is impossible to measure at every point in the flow field simultaneously, the field must be discretized so that a finite number of velocity measurements can approximate the integral equation.

These issues, and many others pertinent to the application of large field turbulent velocity measurements, are presented in this thesis. Also, a hot wire anemometer design which is uniquely adept at multiple channel, low frequency turbulent velocity measurements is presented. The POD reconstruction, which is performed using the velocity measurements made with this hot wire anemometer, and its ability to represent the true dynamics of the large scale structures in the velocity field is shown. Finally, an assessment of the mixing layer models described previously can be made based on the visualization of POD reconstructed velocity field.

Chapter 2

Proper Orthogonal Decomposition

2.1 Introduction

In 1967 Lumley introduced a mathematical technique based on the Karhunen-Loeve expansion to the turbulence community which could be used to extract the most energetic motions in a turbulent flow. This technique, coined the Proper Orthogonal Decomposition or POD, seeks to represent the velocity field into a series of optimal orthogonal functions, optimal in this case referring to the method by which the orthogonal functions are chosen. The first orthogonal function in the POD expansion is "optimized" such that it contains the largest amount of the kinetic energy in the flow and successive functions contain decreasing amounts. By choosing a decomposition of this form, the characteristics of the flow field associated with the mean kinetic energy can be represented by the fewest possible terms. This is in contrast to a Fourier type decomposition where the orthogonal functions are predetermined and are not necessarily reflective of the field; thus, many orthogonal functions must often be utilized to represent the field. Also, because of the nature of the Orthogonal

Decomposition, localized phenomena in the turbulent field can be extracted from the underlying chaotic motion in a way that is not possible by Fourier decompositions.

From the above discussion it is evident that the orthogonal decomposition is a useful tool when one wishes to study the dynamics of large scale turbulent motion. In the task at hand it will prove to be indispensable at reducing the dimensions of the problem and is thus well suited to the task at hand. In this chapter the general form of the POD will be presented as well as the form of the equations for the flow field of interest to this experiment, the axisymmetric mixing layer.

2.2 General Decomposition

The Proper Orthogonal Decomposition seeks the most energetic fluctuations in a random vector field and in the case of a turbulent flow of fluid the vector field of interest is the instantaneous velocity $u_i(\vec{x},t)$. The deterministic functions, $\vartheta_i(\vec{x},t)$ are defined by the maximization of their normalized mean square projection on the velocity vector (Lumley, 1970),

$$\frac{\langle \int u_i(\vec{x},t)\vartheta_i^*(\vec{x},t)d\vec{x} \int \left[u_j(\vec{x}',t)\vartheta_j^*(\vec{x}',t)\right]^* d\vec{x}'dt \rangle}{\int \vartheta_l(\vec{x},t)\vartheta_l^*(\vec{x},t)d\vec{x}dt} = \lambda$$
(2.1)

where the asterisk denotes complex conjugation and angle brackets denote ensemble averaging. The normalization of the projection is done to eliminate amplitude dependence on the resulting functions and instead emphasize the degree of the projection.

The maximization of λ is performed via the calculus of variations and the result is an integral eigenvalue equation of the Fredholm type (Lumley, 1970),

$$\int R_{i,j}(\vec{x}, \vec{x}', t, t') \vartheta_j(\vec{x}', t') d\vec{x}' dt' = \lambda \vartheta_i(\vec{x})$$
(2.2)

where the symmetric kernel of this equation is the two point correlation tensor

$$R_{i,j}(\vec{x}, \vec{x}', t, t') = \langle u_i(\vec{x}, t) u_j(\vec{x}', t') \rangle$$
(2.3)

Since the correlation tensor for this application is Hermitian symmetric, ¹ the solution to the integral eigenvalue equation, eq., 2.2 for finite total energy fields is given by the Hilbert Schmidt theory of linear integral equations. This theory provides a number of useful properties for the set of solutions to eq. 2.2. The most crucial to this application being,

1. There exists a denumerable set of discrete solutions to 2.2 (ϑ_i^n corresponding to the eigenvalues λ^n) where the eigenvalues are real and ordered ($\lambda^1 > \lambda^2 > \lambda^3 \dots$) and 2.2 may be written,

$$\int R_{i,j}(\vec{x}, \vec{x}', t, t') \vartheta_j^n(\vec{x}', t') d\vec{x}' dt' = \lambda^n \vartheta_i^n(\vec{x}) \ (n = 1, 2, 3, \ldots)$$
 (2.4)

where n = 1, 2, 3... represents the discrete nature of the solution set.

2. The eigenfunctions are orthogonal and can be normalized so that

$$\int \vartheta_i^m(\vec{x}, t)\vartheta_i^n(\vec{x}, t)d\vec{x}dt = \delta_{m,n}$$
(2.5)

3. The velocity field can be expressed as a linear combination of the eigenfunctions as

$$u_i(\vec{x},t) = \sum_n a_n \vartheta_i^n(\vec{x},t)$$
 (2.6)

where the random coefficients are obtained using the orthogonality of the *orthonormal* eigenfunctions

$$a_n = \int u_i(\vec{x}, t) \vartheta_i^{n*}(\vec{x}, t) d\vec{x} dt$$
 (2.7)

¹The correlation tensor is symmetric and real, thus it is Hermitian

and coefficients of different orthogonal functions are uncorrelated *i.e.* $\overline{a_p a_q^*} = \lambda^n \delta_{p,q}$) where $\delta_{p,q}$ is the Kroneker delta.

4. The kernel of eq. 2.2 can be expressed using the eigenfunctions and eigenvalues,

$$R_{i,j}(\vec{x}, \vec{x}', t, t') = \sum_{n} \lambda^n \vartheta_i^n(\vec{x}, t) \vartheta_j^{n*}(\vec{x}', t')$$
(2.8)

5. The turbulent kinetic energy is the sum of the eigenvalues (v. 2.5 and 2.6), i.e.,

$$E = \int \langle u_i(\vec{x}, t)u_i(\vec{x}, t) \rangle d\vec{x}dt = \sum_n \lambda^n$$
 (2.9)

The eigenfunctions defined by 2.4 are referred to as characteristic eddies by Lumley (1970) and they contain many of the features given to the so-called coherent structures of turbulence (George, 1988). Note that the eigenfunctions and eigenvalues as determined by eq. 2.4 are deterministic whereas the velocity field and the coefficients, given by eq. 2.7 are random. The significance of the eigenfunctions obtained via the POD can be found in eq. 2.9 where the energy in the flow has been recovered in an optimal manner, as expected. This implies that since the eigenvalues of the expansion are ordered, the first eigenvalue can be identified as a "large eddy" (Townsend, 1956). A summary of the relationship between the POD eigenfunctions and flow structure is given by George (1988) and Moin and Moser (1989).

2.2.1 This Application

The eigenfunctions and eigenvalues of the POD have already been obtained by Glauser (Glauser, 1987) for the axisymmetric mixing layer. The knowledge of the eigenfunctions and eigenvalues for the mixing layer led to the development of a model describing the dynamics of the large scale structures in the mixing layer (v. Glauser et al.

(1995)). However, the eigenfunctions and eigenvalues do not contain enough information to describe the temporal dynamics of the structures because they are stationary and deterministic. Also, since the magnitude of the eigenfunctions is unity (see eq. 2.5) the coefficients, the a_n 's in eq. 2.6, contain all of the amplitude information in the PEA's (a PEA is defined as a Product of the Eigenfunctions and the A's, or coefficients, i.e. $a_n \phi_j^n$) ². The PEA's then are the functions which describe the temporal and spatial evolution of the velocity field in the mixing layer and the first few PEA's describe the evolution of the most energetic of the structures composing the velocity field. It is the goal of this study to experimentally determine all of the functions in the POD expansion for the streamwise component of the velocity field (the eigenfunctions AND coefficients) in the mixing layer of an axisymmetric, turbulent jet.

2.3 Statistically Stationary Directions

The POD, as outlined in the previous section, is developed for vector fields of finite total energy, i.e. statistically inhomogeneous fields. For homogeneous or stationary fields the equations take on a somewhat more complicated form because the orthogonal functions turn out to be harmonic functions of infinite extent. Consequently, the structures defined in these directions are no longer local but rather spread over the entire domain. In this case many terms must be kept in the resulting expansion in order to preserve the nature of the field.

The POD applied in these directions will produce Fourier functions as the orthogonal functions. The most convenient way to decompose these directions is to a priori define the eigenfunctions in these directions to be the harmonic functions and allow

²The author wishes to give credit for the PEA anogram to his advisor upon whom the humor intrinsic to the PEA-POD relation was not lost.

the coefficients to be the familiar Fourier coefficients. This can be accomplished by Fourier transforming the stationary and homogeneous directions in eq. 2.2. Then, the POD can be applied to the coordinate directions which are of finite extent. In the case of a field where the statistics are periodic in one or more directions, the eigenfunctions are still the harmonic functions but are discrete functions of the independent variable.

Let the homogeneous and stationary directions in the flow field be represented by y and the directions of inhomogeneity by x. With these definitions, eq. 2.2 becomes,

$$\int \int R_{i,j}(x,x',y'-y)\vartheta_j^n(x',y')dy'dx' = \lambda^n \vartheta_i^n(x,y)$$
(2.10)

Taking the Fourier transform of both sides of eq. 2.10 and using the convolution property of integrals (Oppenheim and Willsky, 1983) to transform the inside integral yields,

$$\int S_{i,j}(x, x', \vec{k}) \vartheta_j^n(x', \vec{k}) dx' = \Lambda^n(\vec{k}) \vartheta_i(x, \vec{k})$$
(2.11)

where

$$S_{i,j} = \int R_{i,j}(x, x', \vec{p}) e^{(-i2\pi \vec{k} \cdot \vec{p})} d\vec{p}$$
 (2.12)

is the cross spectral tensor, $\vec{p} = y' - y$, is the homogeneous separation vector and the eigenvalue and eigenfunctions have become wave number, \vec{k} , dependent. The original eigenfunctions and eigenvalues can be recovered through the Fourier transformation as shown by eq. 2.12,

$$\lambda^n \Rightarrow \Lambda^n(\vec{k})$$

$$\vartheta_i^n(x,y) \Rightarrow \vartheta_i^n(x,\vec{k})$$

So the integral eigenvalue equation depends only on the direction of inhomogeneity. The directions which are of infinite or periodic extent appear in only a parametric form. This can be as either a continuous dependence for homogeneous directions or discrete as for periodic ones.

2.4 Axisymmetric Mixing Layer

The axisymmetric mixing layer is formed at the exit of a round jet as the high velocity fluid exiting the jet creates a turbulent shear layer with the quiescent fluid outside of the nozzle. A schematic of the axisymmetric mixing layer is shown in fig. 2.1 and the coordinate definitions are $(x_1, x_2, x_3) = (x, r, \theta)$. The integral eigenvalue equation of the POD for the axisymmetric mixing layer would be,

$$\int \int \int R_{i,j}(x,x',r,r',\theta,\theta',t,t')\vartheta_j(x',r',\theta',t')r'dr'd\theta'dt' = \lambda'\vartheta_i(x,r,\theta,t)$$
 (2.13)

For the present analysis, the streamwise coordinate is fixed at a position 3 diameters downstream of the jet exit. Therefore, the streamwise, or x dependence in the functionals of eq. 2.13 is dropped from the following analysis while continuing to recognize its presence.

The velocity field in the mixing layer is statistically stationary in time. Thus, based on the analysis of the previous section, time may be transformed out of the equations. Fourier transforming both sides of eq. 2.13 in time yields,

$$\int \int S_{i,j}(r,r',\theta,\theta',f)\Phi_j(r',\theta',f)r'dr'd\theta' = \Lambda(f)\Phi_i(r,\theta,f)$$
 (2.14)

where,

$$S_{i,j}(r,r',\theta,\theta',f) = \int_{-\infty}^{\infty} R_{i,j}(r,r',\theta,\theta',\tau) e^{(-i2\pi f\tau)} d\tau$$
 (2.15)

$$\Phi_j(r',\theta',f) = \int_{-\infty}^{\infty} \vartheta_j(r',\theta',\tau) e^{(-i2\pi f\tau)} d\tau$$
 (2.16)

where $\tau = t' - t$. Since the time "direction" is of infinite extent, the transformed variables are continuous functions of the frequency f.

The statistical properties of the velocity vector in the azimuthal direction of the mixing layer are axisymmetric (Sreenivasan, 1984) and consequently periodic. The

Figure 2.1: Schematic of the jet mixing layer

orthogonal functions in this direction are then discrete Fourier modes as discussed in the previous section. The kernel of eq. 2.14 may then be expanded in terms of these functions,

$$S_{i,j}(r,r',\theta,\theta',f) = \sum_{m=0}^{\infty} T_{i,j}(r,r',m,f)e^{im(\theta'-\theta)}$$
 (2.17)

and

$$\Phi_j(r,\theta,f) = \sum_{m=0}^{\infty} \psi_j(r,m,f) e^{im(\theta'-\theta)}$$
(2.18)

where m is the azimuthal mode number.

The coefficients in the azimuthal expansions, $T_{i,j}$ and ψ_j are obtained using the orthogonality property of the azimuthal modes,

$$T_{i,j}(r,r',m,f) = \frac{1}{2\pi} \int_0^{2\pi} S_{i,j}(r,r',\theta,\theta',f) e^{im(\theta'-\theta)} d(\theta'-\theta)$$
 (2.19)

and

$$\psi_j(r, m, f) = \frac{1}{2\pi} \int_0^{2\pi} \Phi_j(r, \theta, f) e^{im(\theta' - \theta)} d(\theta' - \theta)$$
(2.20)

Finally, the POD equation becomes,

$$\int T_{i,j}(r,r',m,f)\psi_j(r',m,f)r'dr' = \lambda(m,f)\psi_i(r,m,f)$$
 (2.21)

where λ has remained as the symbol of the eigenvalue but is now an eigenspectra decomposed into azimuthal Fourier modes.

The solution to eq. 2.21 is not straightforward. At first glance it appears that the form of the equation is the same as 2.2 and therefore the Hilbert Schmidt theory should apply to this equation. However, this is not the case because the kernel in eq. 2.21 is not symmetric Hermitian due to the extra r' resulting from the Jacobian of the transformation to polar coordinates. To utilize the Hilbert Schmidt theory the kernel must be recast to make it Hermitian symmetric. This involves dividing the offending metric into two parts, multiplying the entire equation by $r^{1/2}$ and redefining the tensor

and orthogonal function. One can then show that the eigenfunctions obtained from this projection are indeed orthogonal over the rdr plane (see appendix B).

To perform the POD as outlined above, the integral eigenvalue eq. 2.21 is first rearranged to form,

$$\int T_{i,j}(r,r',m,f)r'^{\frac{1}{2}}\psi_j(r',m,f)r'^{\frac{1}{2}}dr' = \lambda(m,f)\psi_i(r,m,f)$$
 (2.22)

multiplying the entire equation by $r^{1/2}$ produces,

$$\int r^{\frac{1}{2}} T_{i,j}(r,r',m,f) r'^{\frac{1}{2}} \psi_j(r',m,f) r'^{\frac{1}{2}} dr' = \lambda(m,f) \psi_i(r,m,f) r^{\frac{1}{2}}$$
 (2.23)

Now redefine the kernel and orthogonal functions to be,

$$W_{i,j}(r,r',m,f) = r^{\frac{1}{2}} T_{i,j}(r,r',m,f) r'^{\frac{1}{2}}$$
(2.24)

and

$$\phi_i(r, m, f) = \psi_i(r, m, f)r^{\frac{1}{2}}$$
(2.25)

thus eq. 2.21 becomes,

$$\int W_{i,j}(r,r',m,f)\phi_j(r',m,f)dr' = \lambda(m,f)\phi_i(r,m,f)$$
 (2.26)

Eq. 2.26 is now a homogeneous integral equation of the second kind. For fixed limits of integration it is referred to as a Fredholm equation and the Hilbert Schmidt theory is applicable. This again provides a series of useful properties of the eigenvalue and eigenfunctions,

1. There exists a denumerable set of discrete solutions to eq. 2.26 (ϕ_i^n corresponding to the eigenvalues λ^n) where the eigenvalues are real and ordered $(\lambda_1(m_o, f_o) > \lambda_2(m_o, f_o) > \lambda_3(m_o, f_o) \dots)$ and eq. 2.26 may be written,

$$\int W_{i,j}(r,r',m,f)\phi_j^n(r',m,f)dr' = \lambda^n(m,f)\phi_i^n(r,m,f)(n=1,2,3,\ldots) \quad (2.27)$$

where n = 1, 2, 3... represents the discrete nature of the solution set.

2. The eigenfunctions are orthogonal and can be normalized so that

$$\int \phi_i^p(r, m, f)\phi_i^q(r, m, f)dr = \delta_{p,q}$$
(2.28)

3. The velocity field, decomposed into azimuthal modes m and frequency f, can be expressed as a linear combination of the eigenfunctions as

$$\hat{u}_i^{nmf}(r, m, f) = \sum_n a_n(m, f)\phi_i^n(r, m, f)$$
 (2.29)

where the random coefficients are obtained using the orthogonality of the eigenfunctions

$$\hat{a}_n(m,f) = \int \hat{u}_i^{nmf}(r,m,f)\phi_i^{n*}(r,m,f)dr$$
 (2.30)

4. The turbulent kinetic energy is the sum of the eigenvalues (v. eq. 2.28 and eq. 2.29)

$$E = \int \langle u_i^{nmf}(r, m, f) u_i^{nmf}(r, m, f) \rangle dr = \sum_{n} \sum_{m} \int_{f} \lambda^n(m, f) df \qquad (2.31)$$

2.4.1 This Application

The streamwise velocity component of the axisymmetric mixing layer will be measured at various radial and azimuthal locations to perform the mathematical operations defined in eqs. 2.27 and 2.30. Since only the streamwise velocity will be measured, the equations simplify to,

$$\int W_{1,1}(r,r',m,f)\phi_1^n(r',m,f)dr' = \lambda^n(m,f)\phi_1^n(r,m,f)$$
 (2.32)

and

$$\hat{a}_n(m,f) = \int \hat{u}_1^{nmf}(r,m,f)\phi_1^{n*}(r,m,f)dr$$
 (2.33)

An important observation here is that unlike eq. 2.32, the kernel of eq. 2.33 is not a statistical quantity but rather an instantaneous realization of the velocity

field which has been decomposed into azimuthal mode numbers. Whereas eq. 2.32 will allow sequential measurements of the velocity field in order to obtain a sufficient statistical measure of the correlation tensor ³, in the recovery of the POD coefficients the streamwise velocity must be measured at all positions of interest *simultaneously* to retain the phase information in the coefficients of eq. 2.33. Therefore a method must be devised to obtain instantaneous and simultaneous measurements of the turbulent velocity field in the mixing layer so that the projection defined by eq. 2.33 can be accomplished.

³This is a result of the stationary nature of the kernel in eq. 2.32.

Chapter 3

Experimental Design

3.1 Introduction

The purpose of this chapter is to introduce the numerical implementation of the POD equations given in chapter 2. First, the numerical approximation of eqs. 2.32 and 2.33 is outlined and then the design considerations which are crucial to the proper discretization of the coefficient projection equation (eq. 2.33) are presented. The position of the hot wire probes in the flow field necessary to recover the pertinent characteristics of the large scale structure dynamics is also discussed. Of particular interest is the design of the hot wire anemometer probes which have long sensing elements to aid in the reduction of spatial aliasing.

3.2 Numerical Approximation

Since the kernel in eq. 2.32 will only be known at discrete positions, the integral in the equation must be replaced by an appropriate quadrature rule. For this application Simpson's 1/3 rule will be used. Discretizing this equation produces for each m,f

combination,

$$\sum_{i=1}^{N_r} W_{1,1}(r_i, r_j) \phi_i^n(r_i) H_i = \lambda^n \phi_1^n(r_j)$$
(3.1)

where N_r is the number of radial measuring positions and H_i is the quadrature weighting.

Eq. 3.1 can be written in the form of a matrix eigenvalue equation (Baker, 1977),

$$WHf = \Lambda f \tag{3.2}$$

where,

$$W = \begin{bmatrix} W_{1,1}(r_1, r_1) & W_{1,1}(r_1, r_2) & \cdots & W_{1,1}(r_1, r_{N_r}) \\ W_{1,1}(r_2, r_1) & W_{1,1}(r_2, r_2) & \cdots & W_{1,1}(r_2, r_{N_r}) \\ \vdots & \ddots & & \vdots \\ W_{1,1}(r_{N_r}, r_1) & W_{1,1}(r_{N_r}, r_2) & \cdots & W_{1,1}(r_{N_r}, r_{N_r}) \end{bmatrix}$$

$$H=\left[egin{array}{c} H_1 \ H_2 \ H_3 \ dots \ H_{N_r} \end{array}
ight]$$

and

$$f = \left[egin{array}{c} \phi_1(r_1) \ \phi_1(r_2) \ \phi_1(r_3) \ dots \ \phi_1(r_{N_r}) \end{array}
ight]$$

Baker (1977) shows that the numerical accuracy of the matrix eigenvalue solution is improved when the coefficient matrix is Hermitian $(X_{i,j} = X_{j,i}^*)$. The matrix WH

is not Hermitian but if both sides of eq. 3.2 are operated on by $H^{1/2}$ the resulting equation will have a Hermitian coefficient matrix, \hat{W} , *i.e.*,

$$\hat{W}\hat{f} = \Lambda \hat{f},\tag{3.3}$$

where

$$\hat{W} = H^{\frac{1}{2}}WH^{\frac{1}{2}} \tag{3.4}$$

is now a Hermitian matrix and,

$$\hat{f} = H^{\frac{1}{2}}f\tag{3.5}$$

Simpson's one-third rule was used for this study and the corresponding H matrix is,

$$H_i = \frac{\Delta r}{3} k_i \tag{3.6}$$

where

$$\Delta r = \frac{(r_o - r_i)}{N_r - 1} \tag{3.7}$$

is the grid spacing in r and $k_i = (1, 4, 2, 4, 2, 1)$ is the Simpson weighting vector.

Following a similar analysis, the equation for the coefficients of the POD eigenfunctions becomes

$$a_n(m,f) = \sum_{i=1}^{N_r} u_1(r_i, m, f) \phi_1^{n*}(r_i, m, f) H_i$$
(3.8)

where the equation is solved using numerical integration. Simpson's one-third rule was again used to define the quadrature weighting function.

3.3 Design Considerations

To solve the integral eigenvalue and coefficient equations (eq. 3.1 and 3.8) experimentally, the instantaneous velocity must be measured at enough points in the flow

field so that the approximation to these equations is optimal. What exactly "enough points" means will become evident shortly, after an introduction to the flow field under investigation is presented.

3.3.1 Flow Field - Azimuthal Direction

The axisymmetric mixing layer is created at the exit of a round jet and continues to approximately 5 diameters downstream where the potential core of the jet disappears and the fully turbulent jet begins. At 3 diameters downstream the mixing layer is a fully developed, turbulent shear layer. In this analysis the extent of the mixing layer at x/d = 3 will be defined as $0.15 \le r/d \le 0.9$ where r is the radial position in the flow and d the diameter of the jet at the exit (v. fig. 2.1). An analysis of the statistical makeup of the axisymmetric mixing layer at x/d = 3 was performed by Glauser $et\ al.\ (1995)$ and his results will be used extensively throughout this section.

In fig. 3.1 (from Glauser *et al.* (1995)) the streamwise velocity correlation measured by Glauser at x/d = 3 is broken into azimuthal Fourier modes,

$$B_{i,j}(r,r',\vartheta) = \frac{1}{2\pi} \int_0^{2\pi} R_{i,j}(r,r',\vartheta) e^{im\vartheta} d\vartheta$$
 (3.9)

where $\vartheta = \theta' - \theta$ is the azimuthal separation. In fig. 3.1 r = r' so that various $B_{i,j}$ can be plotted for each radial position in the jet mixing layer. For i = j = 1, the above decomposition describes the modal distribution of streamwise kinetic energy in the azimuthal direction at x/d = 3. Looking at fig. 3.1 it is easy to see that the statistics of the velocity vector in the high speed (or inner) side of the layer (r/d = 0.1) suggest the presence of strongly correlated azimuthal structures. The low mode number peak of the streamwise kinetic energy near the inner portion of the mixing layer is evidence that a ring like structure exists in that area. As the mixing layer is traversed radially



Figure 3.1: Azimuthal mode number decomposition of the streamwise velocity correlation tensor for r=r', from Glauser et al. (1995)

outward, the kinetic energy in the flow becomes more evenly distributed throughout the azimuthal modes. By the outside of the mixing layer, r/d = 0.8, energy is nearly evenly distributed in all of the modes with modes 4, 5 and 6 containing a larger amount. Up to 16 modes contain some amount of energy suggesting a multi-lobed structure (or structures) exists in this region.

3.3.2 Design Implications

The data presented by Glauser (1995) can be used to determine the number of measurement positions needed to properly resolve the velocity field in the azimuthal direction for the application of the POD. Since this application of the POD seeks only the most energetic of the structures in the flow field, it is not necessary to resolve all of the azimuthal modes present in the flow; it is sufficient to recover only the modes which contribute significantly to the streamwise kinetic energy. For instance, near the potential core of the jet the first three azimuthal modes are sufficient to represent the velocity field in this direction. In the outer portion of the mixing layer upwards of 15 azimuthal modes must be resolved to sufficiently recover the statistics of the velocity field.

A spatial sampling criteria developed by Glauser and George (1992) states that the number of measurement positions necessary in a mode limited field must be at least twice the highest mode present to minimize spatial aliasing, *i.e.*,

where N is the number of measuring positions and m is the highest mode number that can be resolved. Using this criteria, only six measurement positions are necessary to recover the first three modes at the high speed side of the mixing layer and at least 32 positions are required at the low speed side to recover 16 modes.

3.3.3 Flow Field - Radial Direction

The radial direction does not lend itself to Fourier analysis because it is of finite extent so the POD is used in this direction to determine the functions with which to expand. In Glauser's experiment (Glauser, 1987) the POD was performed in the radial direction and his data can be used to determine how many POD modes are necessary to recover the pertinent statistics in this direction. For the streamwise application of the POD, Glauser found that the first eigenmode contained 40% of the turbulent kinetic energy with the second and third eigenmodes contributing another 40%. Thus three eigenmodes recovered 80% of the turbulent kinetic energy. This would certainly indicate that three eigenmodes are sufficient to represent the dynamics of the large scale turbulent structures in the mixing layer. The spatial sampling criteria of Glauser and George suggests 6 measurement positions are necessary in the radial direction to recover these three eigenmodes. Actually, Glauser used seven probes in the radial direction when he performed the POD but it was found that the seventh probe contributed little to the decomposition. Therefore 6 radial positions will be used in the radial direction.

3.4 Probe Array Design

The preceding sections determined the number of probes needed to resolve the flow field to a sufficient level of accuracy for this application. In fig. 3.2 the probe array used in this experiment is shown. There are 6 radial positions and the azimuthal distribution of probes at these radial positions is, starting at the center and proceeding outward, 6, 12, 24, 32, 32, 32 thus providing 138 measurement positions in the mixing later. Each position in the array will contain a single-wire hot-wire anemometer probe

and all will operate simultaneously.

3.4.1 Flow Blockage

Flow blockage was of primary concern with the probe array shown in fig. 3.2. With the transducers used in this experiment however, the blockage was determined to be less than 4\% at the point of the probes main body. The interference at the actual transducer position is considerably less because the probe sensing element is extended forward of the probe body by 0.5 in. The concerns about flow interference downstream of the measurement position due to boundary layer growth and probe cable interference were addressed by utilizing flow visualization techniques to examine the flow field before and after the probes were put into position. Using a smoke wire to mark the fluid flow exiting the round jet, a series of videos were recorded to qualitatively asses the effects of the probe array on the formation of the axisymmetric mixing layer. Specifically, we searched for the instances of flow choking to determine if the probe array impeded flow propagation. Choking was assumed to exist if bent or irregular streamlines were seen entering the probe array. Over the entire range of operation of the smoke wire (0.5 - 10 m/s) no instances of flow choking were observed on the video. Streamlines in the potential core of the jet were straight and virtually unaffected by the presence of the probe array. Therefore, flow blockage effects were determined minimal.

3.4.2 Transducer Design

The transducer used in this experiment is the hot wire anemometer. It was chosen because of its high frequency response, manufacturability and the wealth of information available on its operation. Also, no other technique of global velocity measurements

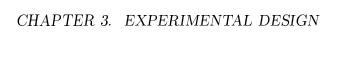


Figure 3.2: Probe array showing location of 138 probes. Note that each circle represents a single-wire hot-wire probe

can operate in the high Reynolds number range of this experiment. The anemometer probes used in this experiment were especially designed for the task at hand and their unique feature is their exaggerated sensing length which is used to reduce the effects of spatial aliasing.

Glauser (1987) found the effects of spatial aliasing to be very misleading if not properly understood. If the velocity field is not sampled at enough positions spatially an aliasing, or folding, problem similar to that found during temporal sampling will occur. A detailed discussion of the pitfalls of spatial aliasing is presented in (Glauser and George, 1992) but an example to elucidate the point is presented here.

Aliasing

Suppose in an experiment there is a periodic signal of spatial frequency f_1^x , that is,

$$X(t) = A\cos(2\pi f_1^x x) \tag{3.10}$$

The Nyquist sampling criteria states that to recover this signal with a digitized version of eq. 3.10, the sampling rate in space must be at least twice f_1^x . *i.e.*,

$$f_c^x = \frac{1}{2\Delta x} \tag{3.11}$$

where f_c^x is the Nyquist frequency which represents the highest frequency recoverable from data sampled at Δx intervals. Suppose the data is sampled at a frequency less than twice the Nyquist frequency, $f_1^x = f_c^x + f_l^x$ where $f_l^x < f_c^x$ then

$$X(n\Delta x) = A\cos(2\pi f_1^x n\Delta x) = A\cos(2\pi f_c^x + 2\pi f_l^x)n\Delta x$$
 (3.12)

substituting in for the definition of the Nyquist frequency,

$$X(n\Delta x) = A\cos(f_c^x - f_l^x)n\Delta x = A\cos(2\pi f_a^x)n\Delta x$$
(3.13)

Figure 3.3: Aliasing example. In this figure $f_1^x = 4m^{-1}$, the data is sampled at 5 m^{-1} which records an aliased spatial frequency $f_a^x = 1m^{-1}$.

where $f_a^x = f_c^x - f_l^x$, and the signal frequency, f_1^x , has become indistinguishable from the original frequency, f_a^x . This phenomenon is called aliasing. Fig. 3.3 shows the above result visually. In the figure, the sampling rate Δx does not provide enough information about $\cos 2\pi f_1^x t$ to recover it faithfully; instead, the sampled result is $\cos 2\pi f_a^x t$ and all of the information in the original frequency is lost. Note that these results are true for any band limited signal. The above results are easily extendable to any "direction" in the field including temporal coordinates ¹ and since in any real field there are not one but a large number of frequencies present, the problem of aliasing can very easily corrupt spectral measurements.

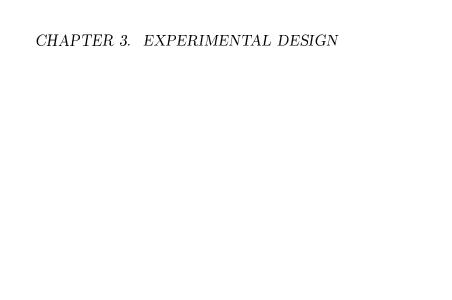


Figure 3.4: Modal decomposition in the jet mixing layer using a 30 point azimuthal resolution, from Glauser (1987)

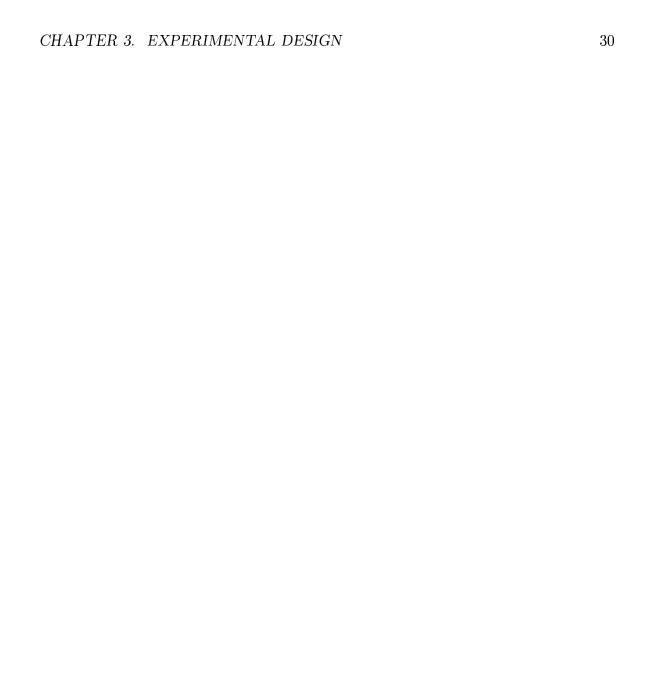


Figure 3.5: Modal decomposition in the jet mixing layer using a 48 point azimuthal resolution, from Glauser (1987)

3.4.3 Aliasing Example in the Mixing Layer

In figs. 3.4 and 3.5 the streamwise azimuthal mode decomposition is shown for two different θ resolutions near the center of the mixing layer (from Glauser (1987)). The first figure shows the decomposition performed using a 30 position resolution and the second a grid of 48 probes. The two plots show a slightly different modal distribution with the lower modes in the 30 point resolution containing more energy and the higher modes less energy than the 48 point figure. This trend is consistent with spatial aliasing phenomena where the higher modes cannot be resolved with a coarse grid and the energy contained in these modes is aliased, or folded, into the lower ones. Thus the modal energy content as shown in fig. 3.4, while close to the actual value, is not quite correct.

The problem of spatial aliasing can be addressed in different ways. The grid spacing can be refined to ensure that all of the modes that contain information are resolved. Often the grid cannot be refined to the point that all important modes can be resolved. In this case it is possible to employ spatial filtering techniques which reduce energy in the higher unresolvable modes *before* sampling to reduce the amount of spatial aliasing.

A spatial filtering technique which can be employed in turbulent velocity measurements is to use the natural spatial filtering property of the hot wire anemometer probe. The probe has a finite size sensing element and thus averages the fluid velocity along its length. This property can be exploited to reduce the effects of spatial aliasing. The difficulty associated with the use of hot wire probes in this manner is there sensing length must be lengthened to gain a noticeable difference in the spatial filtering effect. However, the probes dynamical characteristics in a turbulent field

¹By far the most understood type of aliasing

depend on the flow, specifically, the element responds to shearing forces encountered in a turbulent flow and the heat transfer characteristics can change significantly when the sensing length is much larger than the turbulent scales in the flow. These issues are discussed in the next chapter in which a numerical and experimental investigation into the long sensing element hot wire probe is presented.

Chapter 4

Anemometer Probe Design

4.1 Introduction

The purpose of this chapter is to introduce the long sensing length anemometer probes to be used in the experimental aspect of the present study. Also, a numerical and experimental investigation of the probe characteristics is presented.

4.2 Long Hot Wire Probes

Transducers of any kind always filter the field they are measuring due to their finite size. In the case of hot wire anemometer probes, the sensing element of the wire is the filtering device. Typically when utilizing hot wires to measure turbulent fluid statistics, one is interested in reducing the hot wire length so that all scales in the turbulent fluid are resolved. In the case presented here however, the highest wave numbers (smallest scales) in the turbulent flow do not contribute significantly to the kinetic energy in the flow and are therefore not important. In fact, the information in these scales is undesirable since a spatial grid cannot be employed here to resolve

them. It would be better if they were filtered out before the field was sampled so that the small amount of energy they do contain is not folded into the lower modes. This can be accomplished by using long sensing length hot wire anemometer probes which filter the velocity of the fluid over the length of the probe.

4.3 The Hot Wire as a Spatial Filter

The filtering property of hot wire probes was examined by Wyngaard (1968). In an analytical study using one dimensional spectra, Wyngaard showed that energy in the high wave numbers of isotropic turbulence is attenuated by hot wire probes for all but the smallest sensing length probes. Wyngaard was interested in the effects of the probes sensing length on the *high* wave number turbulent spectra. Since we are interested in the low wave numbers, in the following analysis a model of the turbulent spectrum is used which is representative of all wave numbers in the flow and the effects of spatial aliasing can be studied.

The hot wire anemometer records a voltage signal which is proportional to the velocity of the fluid along the length of the probe. The velocity vector measured by a single hot wire probe of length l may be written as,

$$\vec{u}^m(\vec{x}^m) = \frac{1}{l} \int_{x_2^m - l/2}^{x_2^m + l/2} \vec{u}(x_1^m, x_2, x_3^m) dx_2$$
(4.1)

where \vec{u}^m is the velocity vector measured by the probe, \vec{u} is the true velocity vector and \vec{x}^m is the position of the center of the hot wire probe (see fig 4.1). In eq. 4.1 the probe is oriented parallel to the x_2 axis. Note that eq. 4.1 is just the convolution of the velocity vector with the wire sampling window which in this case is a top hat. Other wire sampling windows could be used such as parabolic or exponential

Figure 4.1: Hot wire anemometer probe

distributions but they are not considered in this analysis.

Representing this integral in Fourier space and manipulating yields (Wyngaard, 1968),

$$\vec{u}^{m}(\vec{x}^{m}) = \int \int_{-\infty}^{\infty} \int \vec{u}(\vec{k}) \exp(i\vec{k} \cdot \vec{x}) \left[\frac{1}{l} \int_{-l/2}^{l/2} \exp(ik_{2}x_{2}) dx_{2} \right] d\vec{k}$$
 (4.2)

where $\vec{k} = (k_1, k_2, k_3)$ is the wave number vector and \vec{u} is the Fourier transform of the true velocity vector. It is assumed that the turbulence is homogeneous so that the flow field can be represented using Fourier transforms in the sense of generalized functions (Lighthill, 1956).

The solution to the integral within the brackets of 4.2 is straightforward and, after evaluating the limits and using the Euler formula for $\sin x$, gives,

$$\vec{u}^m(\vec{x}^m) = \int \int_{-\infty}^{\infty} \int \vec{u}(\vec{k}) \exp(i\vec{k} \cdot \vec{x}) \left[\frac{\sin(k_2 l/2)}{k_2 l/2} \right] d\vec{k}$$
 (4.3)

This is an interesting result because it shows that the velocity measured by the probe is a product of the true velocity and attenuation factor shown in the brackets. The factor in the brackets is the spatial filter which has been imposed by the finite

length of the probe. This term is sometimes called the sink function and its magnitude decreases as the argument, in this case $k_2l/2$ increases. What this means in equation 4.3 is that the measured velocity vector contains less information in the higher wave numbers than is truly present in the field.

Typically, one isn't interested in the velocity but in its correlation and its Fourier transform, the spectrum. The latter of these two can be defined by,

$$F_{11}^{1}(k_1) = \int \int_{-\infty}^{\infty} \Phi_{11}(k_1, k_2, k_3) dk_2 dk_3$$
 (4.4)

where F_{11}^1 is the one dimensional spectrum of the streamwise velocity field and Φ_{11} is the three dimensional spectrum. The notation used follows that of Tennekes and Lumley (1972).

Using the analysis presented in eqs. 4.1 - 4.3, the corresponding one dimensional spectrum as measured by the hot-wire is (Wyngaard, 1968),

$$F_{11}^{1m}(k_1) = \int \int_{-\infty}^{\infty} \Phi_{11}(\vec{k}) \left[\frac{\sin(k_2 l/2)}{k_2 l/2} \right]^2 dk_2 dk_3$$
 (4.5)

Equation 4.5 describes the effects of finite length hot wire probes on turbulent velocity spectra. An experiment was undertaken to study the effectiveness of this model and whether or not the sensing length of the probe attenuated higher wave numbers in the manner outlined in equation 4.5. The results of the experiment were surprising and a numerical investigation was initiated to explain the observed phenomena.

4.4 Experiment

The purpose of the experimental study was to analyze the spatial filtering property of the wire as given in equation 4.5. The experiment involved the measurement of a turbulent velocity field with an extraordinarily long sensing length hot-wire probe. A long hot wire was placed in a turbulent flow field adjacent to three standard length hot wire probes. The idea was to study the effects of the sensing length by determining the spectra of the turbulence with the long wire and comparing that with the turbulent spectra which is obtained with the three short wires which were adjacent and parallel to the long wire; the short wires measuring the turbulent field to a much finer temporal and spatial scale.

4.4.1 Flow field

The turbulent field to be utilized in this analysis is the nearly isotropic field generated behind a wire mesh. A turbulent round jet of diameter 9.8 cm was fitted with a wire mesh which was fixed to the outlet of the jet with a screw clamp. The wire mesh was constructed with 16 threads per inch of 0.0254 cm stainless steel wire. The flow blockage of the mesh was approximately 25 percent. In the operating condition of the jet, the velocity of the fluid immediately downstream of the wire mesh was 16.9 m/s producing a Reynolds number based on mesh thickness of 28,000. The probes were positioned at the center of the jet nozzle to avoid edge effects.

4.4.2 Experimental hardware

The hot wires were made of unplated, 12.7 μm tungsten wire (Sigmund-Cohn, Mt. Vernon, NY) which was welded to in-house probe holders using the DISA 55A12/13 welder and micromanipulator. The probe holders were made using an injection molding technique out of Ciba-Geigy Araldite epoxy in which two 0.05 cm steel music wires were used as leads. In this technique, the steel leads were placed in the middle of a negative mold and held in place with two end plates. The epoxy was injected

Figure 4.2: Probe alignment in 4 wire experiment

into holes drilled into the mold and allowed to cure overnight. After the mold was separated, the probe was extracted and the steel wires were bent to the desired length. The probes were designed to friction fit into standard brass tubing and connectors were constructed out of coaxial cable and pressure connecters so that a tight connection was made between the probe leads and the anemometer cable.

The anemometers used in this study were also made in-house. The description of them is provided elsewhere (v. (Citriniti et al., 1994)) but the essential features of the new design for the present application will be provided. The design of the anemometers follows that of Perry (1982) with some modifications. The characteristics of the Buffalo anemometer are comparable to the DISA M systems with respect to frequency response, signal to noise ratio and stability and are more than adequate for the purposes of this experiment (v. Citriniti et al. (1994)).

The configuration of the hot wires in this experiment is shown in fig 4.2. There were four wires used in all, three of the wires were of standard length $(l/d \approx 200)$ and one was long $(l/d \approx 2,000)$. The long wire was situated directly above the short wires approximately 1 mm away. The three short wires are used to determine the true turbulent field so that a comparison between the turbulent fields as measured by each length wire could be made.

4.4.3 Results of experiment

Figure 4.3 shows the spectra, F_{11}^1 , as measured by the four probes. The data have been smoothed using a 20 % bandwidth filter to facilitate viewing. The data set with the filled box shows the spectra as measured by the long sensing length hot-wire probe. As can be seen by this figure, the energy contained in the higher frequencies has been attenuated by the long sensing length probe. The energy reduction is upwards of

50% in the high frequency region. However, in the low frequency region, the energy in the turbulent spectrum is also reduced by the long wire. From eq. 4.5, the filtering function approaches unity as the argument approaches zero. If the turbulent spectra in figure 4.3 is assumed proportional to the wave number spectra of equation 4.5 then the effect of the filtering function should diminish as the frequency gets smaller. However, the effect of the probe length is seen to attenuate the energy in the low frequencies as well as the high frequencies. The energy in the lower frequencies is attenuated by approximately 20 percent. To investigate this dilemma, a numerical solution to equation 4.5 was initiated.

4.5 Numerical solution

A numerical solution to 4.5 can be formulated once a model for the three dimensional spectrum is provided. If the turbulent field is assumed isotropic, the three dimensional spectrum can be written as (Batchelor, 1953),

$$\Phi_{ij}(\vec{k}) = \frac{E(k)}{4\pi k^4} (k^2 \delta_{ij} - k_i k_j)$$
(4.6)

where k is the magnitude of the wavenumber vector \vec{k} and E(k) is the spectrum function. For evaluation of the integrals in 4.4 and 4.5 the required spectrum is the streamwise three dimensional spectrum given by (Batchelor, 1953),

$$\Phi_{11}(\vec{k}) = \frac{E(k)}{4\pi k^4} \left(1 - \frac{k_1^2}{k^2} \right) \tag{4.7}$$

and the only remaining closure is for E(k).

There are many models for the spectrum function E(k), most of which use the assumption of isotropic turbulence. Pao (1965) developed a model for E(k) for use in the high wave number region of the spectrum. Pao's spectrum model contains the

Figure 4.3: Spectra in 4 wire experiment

exponential roll off characteristic of the high wave number portion of the spectrum. Von Karman (1948) developed a model which is useful in the low wave number region of the spectrum and Helland et al. (1977) combined these two to create a spectrum which models both large and small wave number fluctuations. The model of Helland et al. (1977) satisfies the spectral dissipation constraint of isotropic turbulence presented by Batchelor (1953),

$$2\nu \int_0^\infty k^2 E(k) dk = \epsilon \tag{4.8}$$

and also integrates to give the total turbulent kinetic energy,

$$\int_0^\infty E(k)dk = \frac{3}{2}u^2 \tag{4.9}$$

It is important for this analysis that the spectrum is properly modelled at all wave numbers since it will be integrated over all wave numbers. A plot of the Helland *et al.* (1977) spectrum function is presented in 4.4

The Helland *et al.* (1977) spectrum function, non-dimensionalized by the isotropic dissipation, ϵ , and the integral scale in the flow, \mathcal{L}^{-1} , is given by,

$$\bar{E}(\bar{k}) = \alpha (R_{\mathcal{L}})^{5/4} (\bar{k})^4 [1 + \bar{k}^2]^{-17/6} \exp\left(-\frac{3\alpha}{2R_{\mathcal{L}}} \bar{k}^{4/3}\right)$$
(4.10)

where $\bar{k} = k_1/k$ is the non-dimensional wave number in the k_1 direction, $R_{\mathcal{L}} = \frac{u\mathcal{L}}{\nu}$ is the turbulent Reynolds number and the overbar denotes non-dimensional quantities. The substitutions performed were required to transform the infinite limits in 4.4 and 4.5 to finite limits. The kolmogorov constant, α , was chosen to be 1.6.

The one dimensional spectrum can be non-dimensionalized in a similar manner to yield,

$$\bar{F}_{11}^{1}(\bar{k}_{1}) = \int_{0}^{2\pi} \int_{0}^{1} \frac{\bar{E}(\bar{k})}{4\pi\bar{k}} (1 - \bar{k}^{2}) d\bar{k} d\theta \tag{4.11}$$

¹The parameter \mathcal{L} is not actually the integral scale in the flow but rather a function of it but for the quantitative aspects of this study it is taken as the integral scale.



Figure 4.4: Spectrum function, E(k), of Helland $\it et~al.~(1977)$ with Reynolds number dependence

where θ is a parameter created by the non-dimensionalization and $\bar{k}_1 = k_1 \mathcal{L}$. The non-dimensionalized 1-D spectra is given by,

$$\bar{F}_{11}^{1} = \frac{F_{11}^{1}}{\epsilon^{2/3}} \mathcal{L}^{5/3} \tag{4.12}$$

The first integral in 4.11 can be integrated to obtain,

$$\bar{F}_{11}^{1}(\bar{k}_{1}) = \frac{1}{2} \int_{0}^{1} \frac{\bar{E}(\bar{k})}{\bar{k}} (1 - \bar{k}^{2}) d\bar{k}$$
(4.13)

and the corresponding equation for the filtered spectrum is,

$$\bar{F}_{11}^{1m}(\bar{k}_1) = \int_{0}^{2\pi} \int_{0}^{1} \frac{\bar{E}(\bar{k})}{4\pi\bar{k}} (1 - \bar{k}^2) \left[\frac{\sin\left(\frac{\bar{k}l}{2}\cos\theta\right)}{\bar{k}l\cos\theta/2} \right]^2 d\bar{k}d\theta \tag{4.14}$$

where $\bar{l} = l/\mathcal{L}$ is the non-dimensional wire length.

4.5.1 Numerical solution method

Equations 4.13 and 4.14 were solved with the use of 4.10 using a Gauss-Legendre quadrature method. Gauss quadrature is a very powerful and efficient technique of numerical integration which employs unevenly spaced intervals, optimized by the kernel of the integral. In this application 10 points were used to approximate each integral and the results of the Gauss integration compared favorably with 100 points in a Simpson 1/3 integration scheme but ran in about one tenth the time.

4.5.2 Numerical solution results

The unfiltered one-dimensional spectrum, corresponding to eq. 4.13, and the filtered, or measured, one-dimensional spectrum, given by eq. 4.14, are shown in figure 4.5. As expected, there is less energy in the *measured* (or filtered) one-dimensional spectrum at the high wave numbers than is actually present in the turbulent field. This is

a direct result of the attenuation factor in eq. 4.14. However, another interesting feature in fig. 4.5 is the behavior of the measured spectrum in the low wave number region. Figure 4.6 shows the low wave number region of the spectrum on a linear scale. In it, the difference between the original and measured spectra at the low wave numbers becomes evident. At these low wave numbers it was expected that the true turbulent spectra would be recovered by the hot wire. This was anticipated because the spatial attenuation factor (v. eq. 4.14) approaches unity as the wave number approaches zero. However, it is obvious from fig. 4.5 that this is not the case. After careful consideration it was determined that the answer to this dilemma lies not in the attenuation factor but in the interpretation of the one-dimensional spectra.

The one dimensional spectrum is determined by integrating the three dimensional spectrum, as illustrated by eq. 4.4, since the three dimensional spectrum contains so much information (enough to completely describe the turbulent field). It is this process which has caused the 1-D spectra to appear to contain less energy in the low wave number region of the spectrum. This can be illustrated by examining how the spatial averaging affects the three-dimensional spectrum and how this affect is translated into the one-dimensional spectrum via eq. 4.4 To see this, it is necessary to analyze the three-dimensional spectrum and the process used to create the one-dimensional spectrum.

4.5.3 Three-dimensional spectrum

To facilitate the analysis of the three-dimensional spectrum and the associated onedimensional spectrum, the analysis presented here will focus on the streamwise three dimensional spectrum $\Phi_{11}(\vec{k})$. For isotropic turbulence, surfaces of constant energy for this spectrum are shaped like toroids as shown in fig. 4.7. The gray surfaces

Figure 4.5: Normalized, one dimensional spectra. log-log plot $\,$

 $Figure \ 4.6: \ Normalized, \ one \ dimensional \ spectra. \ log-linear \ plot$

represent shells of constant energy in the filtered three dimensional spectrum (v. eq. 4.5). The light shading on the plane slicing through the shell represents energy in the unfiltered three dimensional spectrum. When the slicing plane is at $k_2 = 0$ there is no light emanating from it indicating that the filtered and unfiltered three dimensional spectra are equivalent at that wave number. As the plane moves down the x_2 axis (the direction aligned with the hot wire probe) the filtering function begins to attenuate the three dimensional spectrum, thus more light is emitted by the slicing plane. Note that in this figure the wire length is fixed at twice the integral scale of the flow. As the plane moves further down the k_2 axis more light is emitted indicating more attenuation by the probe.

The important point to be made by this figure is that at zero wave number the true three dimensional spectrum is recovered by the transducer (v. fig. 4.7 and eq. 4.5). The question then is why does the 1-D spectrum show less energy in the low wave numbers when the 3-D spectrum shows no loss of information in the same range?

To understand why the one dimensional spectra does not recover the true turbulent field in the low wave numbers it is necessary to analyze the definition of the 1-D spectrum. Recall that the 1-D spectrum, $F_{11}^1(k_1)$, is defined by the integral in eq. 4.4 with that from a transducer in the same turbulent field by eq. 4.5. After analyzing eqs. 4.13 and 4.14 it is easy to see that F_{11}^1 is simply the integral of the 3-D spectrum over planes perpendicular to the k_1 direction. In fig. 4.8 the light area on the slicing plane is a visual representation of $F_{11}^1(k_1)$ and the area on the plane bounded by the solid surface represents $F_{11}^{1m}(k_1)$. In the first part of the figure the cutting plane is at $k_1 = 0$. The measured 1-D spectrum at this wave number is smaller (as indicated by the light emitted by the cutting plane) because of the filtering in the k_2 direction by



Figure 4.7: 3-D spectrum for fixed wire length. Gray surface is the filtered 3 dimensional spectrum and shading on cutting plane the energy in the original 3 dimensional spectrum

the finite length hot wire probe 2 . Thus even at $k_1 = 0$ there is a difference between the measured and true 1-D spectrum. However, there is no difference between the measured and true three dimensional spectrum, see fig. 4.9 where the effect of the wire length has been added to the analysis.

In this figure, the gray surface is a contour of a constant energy in the true three dimensional spectrum. The blue shading on the surface represents wave number combinations in which the energy in the true three dimensional spectrum equals that in the measured. Note that the probe is still aligned with the x_2 direction. For a very short sensing length (e.g. a probe length to integral scale ratio of 0.01) the measured and true 3-D spectra are identical as is evident from the amount of blue shading in the first of the surfaces. As the wire length gets larger (l/\mathcal{L} gets larger) the attenuation of the 3-D spectrum increases along the x_2 direction, thus the amount of blue shading decreases in that direction. Note, however, that no matter what the wire length, the blue shading is always present at the lowest value of k_2 . This indicates that the true 3-D spectrum is always recovered at the smallest wave numbers, independent of the probe sensing length. In other words, the statistics of the turbulence are not contaminated by the probe in the 3-D spectrum at the low wave numbers.

The conclusions to be drawn from this analysis are:

- The 1-D spectrum is attenuated by the finite size of the sensing element at virtually every frequency or wave-number. The alignment of the probe and the 1-D spectrum being measured determine how much, and if, attenuation will occur.
- 2. The amount of attenuation produced by the probe increases with probe sensor length.

 $^{^2}$ Recall that the probe is oriented in the x_2 direction



Figure 4.8: 3-D spectrum for fixed wire length. See fig. 4.7 for extended caption



Figure 4.9: 3-D spectrum for various wire lengths. The gray surface is a contour of the unfiltered 3-D spectrum. The shading represents points of equivalent energy in the filtered 3-D spectrum

- 3. The 1-D spectrum can be a very misleading investigative device for the turbulence researcher due to the inability to assess where energy contained at various frequencies or wave numbers comes from.
- 4. The 3-D spectrum will also be attenuated by the probe but the lowest frequencies or wave numbers can be recovered unaffected for even extraordinarily long sensing elements.
- 5. The proper energy spectrum is thus the 3-D spectrum even though its experimental determination is somewhat difficult to obtain.

Finally, since the 3-D spectrum can be recovered faithfully, even for long sensing elements, it is possible to use the finite length of the hot wire anemometer probe to filter the high wave number scales in the turbulent field without fear of losing information in the smallest wave numbers (largest spatial scales). Thus the long sensing element probe can be used to filter out high wave number scales in order to aid in the reduction of spatial aliasing.

4.6 Application to this Experiment

If the hot wire probes used in this experiment are oriented in the azimuthal direction, their filtering property will attenuate energy in the higher azimuthal Fourier mode numbers, as discussed in section 4.3. This property will be exploited later to reduce energy in azimuthal modes which can not be resolved due to the limited number of measuring positions in this direction. The filtering function derived in the section 4.3 will for this alignment be,

$$\kappa = \frac{\sin(k_3 l/2)}{k_3 l/2} \tag{4.15}$$

where k_3 is the wave number in the azimuthal direction. Note that subsequent analyses will focus on the modal energy distribution in the instantaneous velocity field, therefore the term in brackets of 4.15 is raised to unity power. If the circumference of the circle into which the probes are placed is $2\pi r$ then for each azimuthal Fourier mode, m,

$$m\lambda = 2\pi r \tag{4.16}$$

where λ is the wave length of mode m. The wave number in the azimuthal direction is defined by,

$$k_3 = \frac{2\pi}{\lambda} = \frac{m}{r} \tag{4.17}$$

substituting this into eq. 4.15 provides a relationship between the attenuation factor and the azimuthal mode number,

$$\kappa = \left\lceil \frac{\sin\left(\frac{ml}{2r}\right)}{\frac{ml}{2r}} \right\rceil \tag{4.18}$$

As the wire length and radial position in the mixing layer change, so does the attenuation factor, κ . A plot of these variations is shown in fig. 4.10 for a number of l/r ratios. At any fixed radial position in the mixing layer, increasing the probe sensing length will increase the amount of attenuation in the higher modes, *i.e.* κ gets smaller. However, if the sensing length of the probe is fixed at 0.4 in. the following values can be determined,

- Near the potential core $(l/r \sim 0.85)$, $\kappa = 0.75$ when m = 3 indicating that the coefficient multiplying mode 3 is reduced by 25%.
- Near the outer edge of the mixing layer $(l/r \sim 0.15) \kappa = 0.75$ when m = 16.

Fixing the wire length at 0.4 in. will then reduce information in modes which cannot be resolved by the probe distribution shown in fig. 3.2. Specifically, information in

modes higher than 3 near the potential core and modes higher than 17 in the outer portion of the layer are reduced by more than 25 % thus reducing the amount of information folded or aliased. Therefore, the long sensing element hot wire probes can be used to reduce spatial aliaing and have been incorporated in this study.

4.6.1 Heat Transfer Considerations

There are some important concerns when using wires of extended length. The transducer is assumed to be a linear measure of the velocity vector over its length, therefore non-linear effects are not incorporated into its use. In the case of long hot wires, the question of thermal wave propagation in the axial direction of the cylindrical sensing region must be addressed.

Thermal waves are generated by increased heat transfer rates along sections of the sensing region. They can be formed by pockets of shear in the velocity field which occur over a smaller length scale than the sensing element. Since the temperature of the sensing element is assumed to be uniform for proper operation, these effects may render the device ineffective. In a detailed analysis of hot wire probe operation, Corrsin (1963) demonstrated that for probes with an l/d < 1,000 the time scale for axial conduction in a typical hot wire element is substantially higher than the passage of velocity gradients in a subsonic, turbulent shear flow. Since the l/d = 800 here, the effects of shear on the operation of the elements used will be minimal.

Another related concern is the effect of the non-uniform temperature distribution on the operation of the wire. It is known that the temperature distribution along the wire is never uniform since the probe support prongs do not become heated³. If the induced conduction of heat on the wire is substantial, the heat transfer relations

 $^{^{3}}$ The prong to element diameter in this experiment is 40:1 so the prongs can be assumed to be at ambient temperature

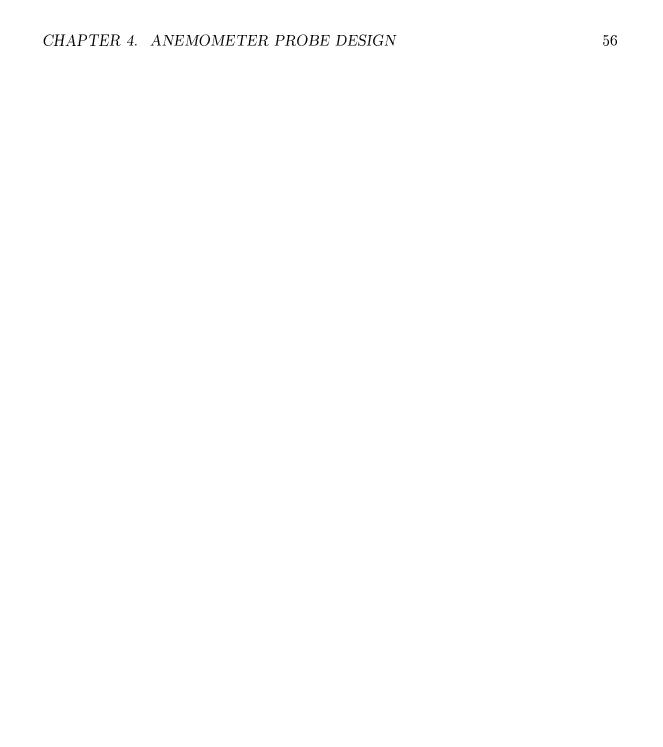


Figure 4.10: Azimuthal mode number filtering caused by hot wire probes oriented in the azimuthal direction

developed for the proper operation of the sensor are invalid. Specifically, it is assumed that conduction along the wire is negligible compared with heat transfer in the radial direction in the wire. If the wires are too short, edge effects could cause this assumption to be suspect. Champagne *et al.* (1967) have shown that for wires with l/d > 200 the end conduction effects are negligibly small. With the wires used here, these concerns can again be neglected.

To determine whether the wires used in this experiment are responsive to the turbulent fluctuations of interest in this experiment, a time scale argument similar to that used by Corrsin (1963) can be made. The time scales important to the operation of the hot wire element are,

$$\tau_1 = \frac{d}{U}$$

$$\tau_2 = \frac{d^2}{\nu}$$

$$\tau_3 = \frac{d^2}{\rho}$$

where d is the element diameter, U is the mean velocity in the flow at the position of the sensor, ν is the kinematic viscosity of the fluid and α is the thermal diffusivity of the fluid. The first time scale represents the time for the flow to sweep past the wire, the second is the time for viscous shear disturbances to diffuse a distance on order of the probe element diameter (i.e., the time for disturbances to diffuse through the wire) and the third time constant is the thermal field response time. To properly operate a hot wire anemometer in a constant temperature mode wherein the probe is calibrated using a steady state method, all three of these time constants must be much smaller than the time scale of the structures convected past the probe (Corrsin, 1963).

Representative structures which are appropriate to this application are large scale

structures and a representative time scale for their convection, assuming these structures are convected with the flow (Townsend, 1956), is given by,

$$\tau_f = \frac{\mathcal{L}}{U_{conv}}$$

where \mathcal{L} is the integral scale of the flow. In the experimental setup at hand the following properties are known:

d	$12.7x10^{-6}m.$
U	12m/s
ν	$15.9x10^{-6}m^2/s$
α	$22.5x10^{-6}m^2/s$

substituting these values into the various time constants yields,

$$\tau_1 = 1.06x10^{-6}s.$$

$$\tau_2 = 1.01x10^{-5}s.$$

$$\tau_3 = 7.17x10^{-6}s.$$

$$\tau_f = \frac{0.098m.}{12m/s} = 8.17x10^{-3}$$

where the integral scale is assumed on order of the jet diameter. It is apparent from this order of magnitude study that the hot wire responds in a sufficiently fast manner $(\tau_f \gg \tau_i, i = 1, 2, 3)$. Also, these numbers suggest that a steady state calibration of mean velocity and voltage will be sufficient to recover the statistics of the velocity field.

Chapter 5

Experiment

5.1 Introduction

The purpose of this chapter is to introduce the facility which will create the axisymmetric mixing layer as well as the experimental apparatus used to make the velocity measurements. Of particular interest is the hot wire anemometer circuitry which was specifically designed to handle the multiple simultaneous measurements in this experiment.

5.2 Facility

The turbulent mixing layer used in this experiment is generated by an isothermal, non-reacting, incompressible, single-phase axisymmetric jet, which is shown schematically in 5.1. The details of the design are given in (Khwaja, 1981) and (Glauser, 1987). The blower is a Dayton model No. 4C108 with a $10\frac{5}{8}$ in. wheel which contains 6 impellers. Driving the blower is a 1 HP 3 phase AC motor which is controlled with a Graham A.C. motor controller model #1540-AFC5. The diffuser and settling

Figure 5.1: Experimental jet facility, from Glauser (1987)

chamber contain 7-20 mesh 25% solidity screens and 1-30 mesh 35% solidity screen and two sections of honeycombs, made of drinking straws, to eliminate any large scale disturbances created by the impeller. At the end of the settling chamber is a fifth order polynomial contraction nozzle. The area ratio between the settling chamber and exit plane is 10:1 providing an exit diameter of 0.098 m.

The jet facility can create exit velocities from 0.5 m/s to 40 m/s. For this experiment, the exit velocity is 12.5m/s which translates to a Reynolds number based on exit diameter of 80,000. The turbulence intensity at the jet exit is 0.35% and the boundary layer at the jet exit was turbulent with an approximate thickness of 0.0012 m. The mean velocity profile is flat to within 0.1%. The measurements will be made at a position 3 diameters downstream of the jet exit. This position was chosen because it is representative of the fully developed mixing layer but it is by no means special. The range of 1 < x/d < 5 is approximately self-preserving and the transition to turbulence occurs before x/d = 1.

5.3 Instrumentation

The single-wire probes used for this study were constructed in-house using an injection molding technique with Ciba-Geigy Archery Bow epoxy. Tempered steel music wires with a diameter of 0.020 in. were used as the support prongs and were held securely between two halves of a plexiglass mold using aluminum guides. The molds had a cylindrical probe shape machined into them so that when connected the probe body formed inside (v. fig. 5.2). The probe manufacturing process began with the cleaning of the plexiglass molds with isopropyl alcohol and then waxing with three coats of Carnauba Cream boat wax. Carnauba wax was used because it did not contain silicon

Figure 5.2: Hot wire probe mold, (mating plexiglass piece not shown)

which was found to foster attachment of the epoxy to the plexiglass. After cleaning and waxing the mold the Poly-Vinyl Alcohol was appled to facilitate the removal of the epoxy from the mold upon curing. The two halves of the mold were fastened together and the epoxy was injected using a 10 cc syringe through the injection hole until the bleeder hole was nearly filled. A total of 6 cc. of the epoxy was necessary for the 6 probe molds used. The molds were then placed in a 70° C water bath to reduce curing time from 24 hours to 1 hour. After the epoxy cured the molds were extracted and separated and the probe was removed and cleaned. The steel support prongs were then cleaned and bent to 0.4 in. separation distance using an aluminum chuck which ensured that all probes were bent to the same specifications.

The probe body is comprised of two sections. The section closest to the sensing element was 0.1 in. in diameter which is the same thickness as the brass tubing (0.1) in. OD x 0.007 in. wall x 12 in. long) which is used as the probe support. This eliminated aerodynamic disturbances which could be generated by the seam between the probe and the support tube. The second section of the probe body has a diameter of 0.81 in. and fits snugly into the support tube. The two steel support prongs are deliberately set off center in this section such that one prong passed directly down

the center of the cylinder and the other protrudes slightly out of the cylinder to make contact with the brass tubing. This is done so that the brass tubing could be used as the return lead for the anemometer probe operation. Typically, there are two separate leads entering a probe support tube but it was necessary to minimize the probes cross sectional area to reduce the effects of flow blockage.

The single lead exiting the center of the probe body was pressure fitted into a gold plated surface mount socket (Samtec SC-2SI-GT) which was in turn soldered to the center lead of RG-174/U coaxial cable. The shield on the coaxial cable was secured to the outside of the brass support tube using shrink wrap thus completing the line-return circuit for the probe. Five meter cables were used to connect the probes to the anemometers.

The probes sensing element was 0.4 in. long and made of unplated 12.7 μ m. tungsten wire (Sigmund-Cohn, Mt. Vernon, NY) thus producing a length to diameter ratio of approximately 800. The wire was welded to the probe support prongs described in the previous section using the Dantec 55A12/13 micromanipulator and welder. The probes were operated in the constant temperature mode using a custom hot wire anemometer circuit at an overheat of $\frac{T_w}{T_a} = 1.8$.

5.3.1 Sampling overview

Turbulent Field

Before statistics of the velocity field can be measured it is important to know the statistical range of the field of interest as well as the capabilities of the measuring device. The spatial sampling criteria necessary for the proper discretization of the velocity field were laid out in chapter 3 and in this section the temporal characteristics of the velocity field will be examined. The maximum frequency of interest in a

turbulent field is best estimated by the Kolmogorov scale, η ,

$$f_k = \frac{U_c}{2\pi\eta} \tag{5.1}$$

For the parameters in this experiment the maximum frequency as given by eq. 5.1 would be approximately 6450 Hz. The sampling rate necessary to avoid aliasing of the digitized signal (v. Hardin (1986)) would be twice this number or 12,900 Hz. This value is representative of the turbulent velocity field alone and does not consider the attenuation effects of the measuring device.

Measuring Device

The hot wire transducer can respond to fluctuating velocities only if the period of the fluctuations is greater than twice the probe length. This is a result of the fact that the probe averages the velocity field along its length (see section 4.3). Using this fact, a maximum resolvable frequency can be estimated for the hot wire probe as,

$$f_p = \frac{U_c}{2l_m} \tag{5.2}$$

where l_w is the probe wire length. For the parameters in this experiment, $f_p = 600$ Hz. This upper frequency bound may appear at first glance to be very limiting, especially when the maximum frequency in the flow was estimated to be near 13 kHz. but because the intent of this experiment is to study the energy containing portion of the flow, the maximum frequency of interest is much smaller than 13 kHz. To elucidate this point a spectrum was measured in the middle of the axisymmetric mixing layer with a probe with an l/d = 200 using a Dantec 55M10 constant temperature anemometer. The result is shown in fig. 5.3. As the figure shows, the energy content in the flow has decreased by over one decade at a frequency of 500 Hz. This

Figure 5.3: Spectrum from the mixing layer of the axisymmetric jet at $Re_D=80,000$

frequency is well into the $k^{-5/3}$ range of the spectrum and therefore contributes little to the mean kinetic energy of the flow.

It would be unproductive to resolve frequencies in the spectrum greater than about 800 Hz. so low pass, anti-aliasing filters were used in the experiment to filter fluctuations higher than 800 Hz. Accordingly, the sampling rate of the individual anemometers must be greater than 1600 Hz. to avoid temporal aliasing. The actual sampling rate of the individual anemometer channels was set at 2,048 Hz. and the record length of each block of data was 1024 samples giving a bandwidth of 2 Hz. and a length of 0.5 sec. To reduce the variability of the statistics in this experiment there were 300 such blocks measured and this reduced the variability to approximately 5 percent ¹. The blocks of data were separated by at least one integral scale to insure that they each make an independent contribution to the statistical measure (George et al., 1978).

5.3.2 Calibration

Calibration of single wire probes consists of measuring the output voltage of the anemometer over a range of known velocities normal to the wire. The voltage data is then converted to velocity units by fitting a polynomial (George et al., 1987) function to the raw voltage data. The response equation has the form,

$$U_{eff}^{p} = \sum_{n=0}^{N} a_n E^n \tag{5.3}$$

where U_{eff} is the effective velocity measured by the probe and N determines the order of the fit. The advantage of using a calibration such as this over a King's Law approach is that least squares optimization can be directly applied to eq. 5.3 and the

The variability in a random system goes approximately as $\epsilon \sim 1/\sqrt{n}$ where n is the number of independent realizations (George et al., 1978)

principle uncertainty in the fit lies with U. Also, since the desired quantity is the velocity, U, it can be easily obtained from eq. 5.3 by simple multiplication; *i.e.* no inversion techniques are necessary which divide the uncertainty in the quantities to all terms.

The velocity of the fluid at the jet exit was inferred from the plenum pressure using Bernoulli's equation. The pressure was recorded in a digitized form by a Validyne DP103-14 pressure transducer and model CD23 Carrier Demodulator. The pressure transducer was calibrated against a Meriam Instrument Co. Model 34FB2 micromanometer which had an accuracy of 0.001 in. of water. The jet was allowed to run for at least one hour before calibration so that an isothermal environment was established. The voltages were digitized using a Phoenix Data Inc. simultaneous sample and hold, 15 bit analog to digital computer (A/D) and the data was stored in a SUN Microsystems SUN4/60 computer via DMA routines. The maximum sampling rate of the A/D is 325 KHz which when divided by the number of channels of anemometry yields the maximum sampling rate of each channel. The sampling rate used for this experiment was 2,048 Hz.

The procedure for calibrating the probes was as follows. The hot wire probe array (refer to fig. 3.2) was placed in the flow 4 mm downstream of the jet exit plane described in section 5.2. The velocity of the fluid at the jet exit is flat to within 0.1% and the boundary layer was small enough so that the jet was assumed to provide a constant, laminar flow for calibration. Since the exit diameter of the round jet is smaller than the diameter of the probe array, a series of 5 calibrations was necessary. The array was positioned so that the maximum number of probes could be calibrated at each of the 5 positions. By varying the exit velocity of the jet and recording the voltage output by each anemometer, a series of data points were obtained and the

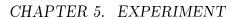
coefficients in eq. 5.3 were calculated. Typical errors between the calibrated and measured velocities were less than 0.2%. For this experiment, p = 0.5 and N = 3. A set of calibration curves using this polynomial fit is given in fig. 5.4.

5.4 Anemometry

Because of the large number of hot wire probes needed in this experiment (138), commercial anemometers were deemed cost prohibitive (upwards of \$20,000 for 16 channels). So a team at SUNY Buffalo designed, manufactured and tested a less expensive but equally effective hot wire anemometer circuit. The anemometer that was produced was a compact (16 of them fit on a 9 in. x 11 in. circuit board) inexpensive (less than \$50 per anemometer including all hardware costs) and effective (typical circuit performance equals that of the Dantec M systems) anemometer system.

The design goals for the circuit were relatively modest. The maximum frequency of interest in the flow is at 800 Hz. and thus the sampling rate necessary for each anemometer channel is only about 1600 Hz. Therefore, the extra circuitry found in most commercial anemometer systems which boosts frequency response into the 50-60 kHz. range is unnecessary for this application. This relaxation of the frequency response requirement for the circuit allowed for a number of innovative ideas which proved useful for the gathering of large amounts of data.

The anemometer circuit was built around the feedback loop discussed in Perry (1982). It was chosen because of its simplicity and extensive documentation. It requires only two operational amplifiers and a Wheatstone bridge, lends itself readily to the numerous anemometers required, and possesses a frequency response which far exceeds the requirements of this study.



69

Figure 5.4: Sample of calibration data (shown as symbols) and the corresponding polynomial fit (solid lines)

5.4.1 Feedback loop

The principal component in the circuit is a Wheatstone bridge with a bridge resistance ratio of 10:1 (v. fig. 5.5). Two low noise, wide bandwidth operational amplifiers (National LF347 Quad JFET) are used to amplify the bridge unbalance voltage. The second of the two has an adjustable offset voltage which starts the feedback operation and controls the tuning of the frequency response in the feedback loop. The open-loop voltage gain for both op-amps is 10^5 . A Darlington transistor, which follows the second op-amp, is used to boost the current in the feedback loop in order to drive enough current to heat the long sensing element hot wires to their overheat state. The hot wires, operating at their overheat value drew 200mA per anemometer channel from the power supply driving the bridge. The bridge is driven off balance by a Clarostat 200 Ω adjustable potentiometer. The voltages used to power the op-amps and transistor were +15 V and -15V and the +15 V was also used to power the bridge through the transistor.

There are no adjustments available in the feedback loop to compensate for cable inductance or capacitance because these effects were found insignificant during preliminary testing. In particular, during the initial design phase cable compensation was included and the increased frequency response attained with the cable compensation was less than 3% based on overshoot estimates using a square wave test. Also, the stability of the circuit was not affected by the presence of the cable compensation to a sufficient degree as to warrant their inclusion in the circuit. The numerous channels of anemometry would require individual tuning of the compensating devices and this would not only be tedious but the phase differences induced between channels would be detrimental to the simultaneous acquisition of data. The frequency response can be improved by adjustment of the offset voltage on the second operational amplifier,

Figure 5.5: Anemometer circuit diagram

and this provided sufficient adjustment for the frequency response tuning.

5.4.2 Output stage

The bridge-top voltage is fed into an 8th order, low pass Bessel filter (MAXIM - MAX296) to prevent aliasing of temporal signals due to the low overall sampling rate of the each anemometer channel. The corner frequency of the filter is set with an external function generator and has a range of 0.1 to 25 kHz. The filters have a 48 dB per octave roll off and their phase angle is linear in frequency. This last property is critical to the operation at hand because all 138 anemometers must sample the velocity field simultaneously. Other filters, (e.g. Butterworth filters) have non-linear phase shift properties making it difficult to insure that all measurements are made simultaneously. With a linear phase shift the effect of the filter on the velocity measurement is simply to impose a phase lag and all anemometers experience the same lag. This property is best explained with an example.

If the low pass filter is imagined to be a black box with the velocity (or voltage) signal entering, the signal leaving the box will be a phase shifted and amplitude modified version of the input,

$$\hat{u}(f) \to \boxed{\text{FILTER}} \to A(f)e^{i\phi(f)}\hat{u}(f)$$
 (5.4)

where $\hat{u}(f)$ is the Fourier transformed velocity vector, A(f) is the amplitude modulation, $\phi(f)$ is the phase shift introduced by the filter and i is $\sqrt{-1}$. Let $\hat{u}_f(f) = e^{(i\phi(f))}\hat{u}(f)$ be the output of the black box. Using the definition of the Fourier transform,

$$u_f(t) = \int_{-\infty}^{\infty} e^{-i2\pi f t} \hat{u}_f(f) df$$
 (5.5)

and substituting for $\hat{u}_f(f)$ yields

$$u_f(t) = \int_{-\infty}^{\infty} e^{-i2\pi f t} e^{i\phi(f)} \hat{u}(f) df.$$
 (5.6)

The linear phase shift property of the Bessel filter implies

$$\phi = 2\pi q f \tag{5.7}$$

where q is the slope of the phase shift. Combining eqs. 5.6 and 5.7 gives,

$$u_f(t) = \int_{-\infty}^{\infty} e^{-i2\pi f(t-q)} A(f) \hat{u}_f(f) df$$

$$(5.8)$$

The presence of the (t-q) term in 5.8 shows that the linear phase shift of the Bessel filter merely adds a constant time lag to all velocity measurements. Thus, if all filters are phase matched, the net effect of the Bessel filters is to delay all signals by the same time constant. In fact if A(f) = 1,

$$\hat{u}_f(t) = u(t - q) \tag{5.9}$$

After the Bessel filter stage, the voltage is passed into an output control section, the purpose of which is to adjust the output voltage range and level so that it can be read by the A/D in the lab at SUNY Buffalo which has a maximum input range of -10V to +10V. Adjusting the output control voltage (Voc) and the trim potentiometer in the output control stage of the circuit provides a way to maximize sensitivity of the analog to digital conversion. The sensitivity of the A/D is determined by the input voltage range and the number of bits available for conversions (15 for the A/D at SUNY Buffalo). For the 20V range and 15 bit resolution the sensitivity for the A/D is, $S = \Delta V/2^n = 20V/2^{15} = 6.1035x10^{-4}V/bit$. The smaller S gets the more effect quantization noise influences the output signal. To maximize the sensitivity,

the full voltage range of the A/D should be utilized. For this experiment, the typical operating range was only 4V, but this provided enough range to minimize the effect of quantization noise while avoiding clipping (Tan-atichat and George, 1985).

The final components on the output stage of the anemometer circuit are the sample and hold and multiplexer. Both devices are normally found on the A/D and not the anemometer. Because we were interested in 138 simultaneous measurements and A/D channels are not cheap, it was desirable to reduce the required number of A/D channels by multiplexing all anemometers on a board through a single A/D channel. By placing the sample and hold on the anemometer, it was possible to simultaneously sample all probes and then multiplex all the anemometer channels on a single board to one A/D channel. The A/D scanned the boards at a high rate, taking one sample from each board per pass. When the A/D had completed a scan of its channels, it could increment the multiplexer on each anemometer board to the next anemometer channel. In this way, all channels on all boards could be digitized. This great reduction in hardware was possible because the throughput rate of the Phoenix A/D (325 kHz) was much greater than the sampling rate of the individual channels (2 kHz).

It was decided, because of typical micro-chip construction, that 16 anemometers would be placed on a single circuit board. The duty of the multiplexer is to select a single anemometer signal out of 16 to be sent to the A/D. The 16 channel differential analog multiplexers (Analog Devices - MUX16FP) are fabricated with Bipolar-JFET technology and the channel addressing is controlled by a 4 bit binary switch. With 16 anemometers per board a total of nine full boards were required. This provided a total of 144 anemometers, but only 138 were utilized.

To ensure simultaneous acquisition of velocity measurements, each anemometer

required a sample and hold. The sample and hold is a circuit device which, when directed, will hold the current value of the input voltage for a finite length of time 2 . The sample and holds circuits used here are Burr Brown 12 bit DIP design (SHC298) with less than 10μ s. acquisition time, a low droop rate (1mV/ms) and an aperture time of 200 ns.

5.4.3 Construction and assembly

The 16 anemometers are arranged on the circuit board in three rows of five with one channel in the lower left section of the board (see fig. 5.6). The multiplexer, input power connections and lines to a digital control board are located on the bottom of the board. The circuit photo-plot artwork was performed by Circuit Design Services in Buffalo, NY and the board manufacturing and component population by Buffalo Circuits also located in Buffalo. The boards are 22.86 cm. (9 in.) wide and 27.94 cm. (11in.) long and are composed of three layers. The first layer is the solder layer (bottom) of the board is the side which is placed in the solder tank for component soldering. The second layer (top) contains the horizontal circuit traces and is the side of the board containing all of the circuit components. The third layer is the silk screen layer which marks all of the components on the top side of the board. There is a solder barrier covering both sides of the board which prevents cold soldering of any lines not meant to be connected. Two of the photo plots are presented in figs. 5.7 and 5.8 which show the top and bottom layers of the board.

Figure 5.6: Picture of 16 channel anemometer board

Figure 5.7: Photo plot of board layer 1

Figure 5.8: Photo plot of board layer 2

Figure 5.9: Picture of an emometer board housing

Figure 5.10: Circuit diagram of digital control board

Figure 5.11: Timing diagram for digital control board and A/D

5.4.4 Anemometer Board Housing

The 9 boards of 16 anemometers are attached to aluminum front plates which are mounted on a vertical rack (v. fig. 5.9). The aluminum plates have holes drilled in them so that the two trim pots controlling overheat adjustment and output control can be reached. Also, there are two more holes per channel on the front panels for access to the bridge top and wire top voltages. The boards are arranged two per plate with the top plate containing only one board. The other half of the top plate contains the power switch, the communication lines to the A/D, the manual override switch for the sample and hold and a hard-wired binary addressing system for the multiplexer to allow for manual testing of individual channels.

One additional component is necessary to control the timing of the circuit, the digital control board (v. fig. 5.10). The digital control board (DCB) is the brains of the anemometer operation, it controls the timing of the MUX, the sample and hold's and the A/D. The timing for the circuit is critical to its operation so a description of the timing process is presented. When the user is ready to begin sampling data a GO pulse is issued from the A/D (v. fig. 5.11). The GO pulse resets the entire system such that each MUX sets its analog switch to the first anemometer channel on each of the 9 boards of 16 channels ³. The sample and hold on each anemometer is then instructed to hold the current value in its register (which is the output voltage of the anemometer it is connected to). The digital control board then sends a pulse to the A/D to begin sampling all of its 9 connections. After reading all 9 channels the A/D sends an EOS (end of scan) pulse to the DCB and the DCB instructs the MUX's to switch to channel 2 on each board. The sampling process is repeated until

 $^{^2\}mathrm{In}$ a typical application the sample and hold will hold the input value with a accuracy of up to $5\mathrm{mV/minute}$

³ All boards are set up in parallel so that when one board receives a signal, all receive it.

the voltages from all 16 anemometers on all 9 boards are read.

During the data acquisition phase the sample and holds maintain their value and since all sample and hold chips are strobed simultaneously, all channels of anemometry record the voltage measurement at the same instant. Therefore all measure the velocity at the same instant. In summary, all channels are sampled simultaneously, then held and read by the A/D when convenient. This is possible because the low overall sampling rate for each anemometer (2,048 Hz) is less than the maximum attainable frequency of the A/D (325 kHz). ÷ 144 channels = 2257 Hz. maximum per channel).

5.4.5 Operation

The process of setting up and operating each channel of anemometry proceeded as follows: The probes were inserted into their positions on the probe array 3.2 and connected to the BNC connectors on the aluminum front plates of the cabinet. Once the probe is connected it is ready for operation. There is no way to compensate for the probe cable resistance so the overheat can not be adjusted as on most commercial systems. The cold resistance of the cables, R_c must be measured and subtracted off the wire resistance as the final step in calculating the wires hot resistance. In this configuration the bridge is never really "zero-balanced".

The hot resistance of the wire, necessary to calculate the overheat ratio, is measured while the wire is in operation. This is accomplished by measuring the bridge top voltage, V_t , the wire top voltage, V_w , and using Ohm's Law to calculate the hot resistance, R_w , of the wire (v. fig. 5.12),

$$R_w = \frac{V_w}{I_w} \tag{5.10}$$

Figure 5.12: Sketch of Wheatstone bridge

where I_w is the current in the probe arm of the bridge. The current through the hot wire is calculated using the bridge top current,

$$I_w = \frac{V_t - V_w}{R_2} {(5.11)}$$

Once the hot resistance of the wire is calculated, the cable resistance R_c is subtracted off and the overheat ratio can be calculated,

$$OH = \frac{(R_w - R_c)}{R_{cold}} = 1.8 (5.12)$$

where R_{cold} is the cold resistance of the probe. All information is now available to calculate the overheat ratio via 5.12. The overheat ratio is calculated and if it is not 1.8 the bridge resistance, R_3 in fig.5.12, is adjusted until it reaches 1.8. Typical values

for the parameters listed are given below.

$$R_{cold} = 4.88\Omega$$
 $R_{w} = 8.79\Omega$
 $R_{c} = 1.92\Omega$
 $V_{w} = 1.90V$
 $V_{t} = 6.35V$
 $V_{os} = -.475V$. (5.13)

5.4.6 Circuit performance

The individual anemometers were tested in the lab at SUNY Buffalo to determine their performance characteristics. The frequency response of the anemometers was determined using a square wave test with a hot wire probe in a uniform laminar flow field. The frequency response was calculated using Freymuth's equation (Freymuth, 1977),

$$f_k = \frac{1}{1.3\tau} \tag{5.14}$$

where τ is the time for the anemometer to respond to the rising or falling edge of the square wave (Freymuth, 1977). The test parameters were,

$$l/d = 200$$

$$d = 5\mu m.$$

$$U_{exit} = 10m/s$$

$$f_{corner} = 20kHz$$

$$(5.15)$$

The laminar flow field used was the potential core of an axisymmetric jet. A square wave was fed into the bridge circuit at the wire top and ground points of the Wheat-stone bridge (v. fig.5.12), in parallel with the hot wire probe as discussed in Freymuth (1977). The principle behind the test is an electronic pulse produced by the square

86

Figure 5.13: Spectra in mixing layer of jet using the Buffalo and Dantec anemometers

wave generator is indistinguishable from a real velocity pulse by the bridge and the frequency response of the bridge can be measured without a true velocity pulse in the flow. The square wave test for the Buffalo anemometers produced a frequency response of about 12 kHz. This value may appear low but it can be increased by using a smaller wire and placing the probe in a higher mean flow. For the purposes of the measurements at hand⁴ this frequency response is more than sufficient.

To insure that the anemometers were working correctly, a test was devised wherein the Buffalo anemometer was compared with an industry benchmark, the Dantec 55M anemometer. A spectrum of the turbulence in the axisymmetric mixing layer was made with the two anemometers and the results are shown in fig. 5.13. The spectra recovered by the two anemometers are identical up until about 2 kHz. At this point the Dantec unit appears to extend the frequency range of the spectrum while the Buffalo anemometer attenuates the spectrum past this frequency. However, the apparent gain in frequency response by the Dantec system is a result of a frequency compensation circut which Dantec adds to their systems. The Dantec units add an amplification section to their output conditioners which causes the output to be amplified by a +6 dB per octave ramp function. This compensation assumes the roll off in the frequency domain is due to inadequate temporal resolution which is a -6dB per octave, but only for hot wires. The compensation unit cancels out this roll off and increases the effective frequency response of the anemometer. This effect can be easily demonstrated by operating the anemometer in the hot film mode where the compensating circuit corrects for a -3dB/octave roll off (since hot films roll off at -3dB per octave). In this case the effective frequency response is again extended but because the hot wire does not roll off at the same rate as the hot film, the Dantec

⁴In fact many of todays experiments would be suited by these anemometers

circuit over compensates for the thermal lag induced roll off (see fig. 5.13). Now, in fact, in many applications, the spectral roll-off is not due to thermal lag, but due to spatial resolution of the wire. And it is not a -6dB roll-off but an unknown amount determined by the turbulence being measured (v. Wyngaard (1968)). Thus, the roll off in the spectrum after 2 kHz. is due to the length of the probe because it is unable to resolve the turbulent scales at these frequencies. The frequency at which the probe can no longer resolve the scales of the turbulence is,

$$f_k = \frac{U_c}{2l} \tag{5.16}$$

using the parameters of the test, the probe roll off should be near 1600 Hz. This is approximately where the Buffalo anemometer begins rolling off. Therefore, it appears that the Buffalo anemometer provides a more accurate measure of the true turbulent field, and the apparently greater frequency response of the Dantec anemometer is simply the anemometer compensating for the wrong thing.

5.4.7 Circuit noise properties

Considerable effort was made to keep the noise in the circuit to a minimum. The circuit board design provides a clean connection for all components. A large ground plane was absolutely essential to eliminate external noise and cross talk. This is because the large number of channels and the high current draw from each long hot wire could create voltage differences in the ground with its small, but finite, resistivity.

The cabinet which houses the anemometer boards was grounded to a building ground which was separate from the analog ground of the anemometers. The power supplies in the cabinet were shielded from the boards with a section of aluminum flashing which was connected to the cabinet ground. Each anemometer board had its

Figure 5.14: Coherence in mixing layer of jet using the Buffalo anemometer

CHAPTER 5. EXPERIMENT

90

own analog ground connection using 10 gauge wire so there were no internal ground loops between boards. A careful ground network was installed, including a brass strip which acted as the trunk of the grounding tree. The triax cables connecting the output of the MUX to the A/D⁵ were used so that the outside shield could protect the twisted pair leads from external noise. The shield was grounded at the anemometer cabinet so that no ground loops existed between the cabinet and the A/D. The A/D inputs are differential and the analog ground is separate from the power ground so there were no ground loops through the building either.

To test the anemometer noise properties the Dantec 55M system was again employed. The two anemometers were connected to the same probe which was placed in a laminar flow field (the potential core of the jet) of 10 m/s. The output rms voltage of each anemometer was calculated using a Dantec 55D35 rms voltmeter and the results show a reduction in noise level for the Buffalo anemometer.

 $V_{rms} = 12.15 mV$ Buffalo anemometer

 $V_{rms} = 19.10 mV$ Dantec anemometer

Since part of the difference in the rms measurements could be attributed to the linear bandwidth of the Buffalo anemometer, the spectral level of the noise was further examined. This can be determined by analyzing the value of the spectrum in the highest frequency. Since there is no energy in the spectrum at the very high frequencies the energy content there must be noise. Fig. 5.13 shows the difference between the Buffalo and Dantec spectral noise levels. The higher noise level in the Dantec anemometer can be attributed to the compensation unit discussed earlier which

⁵These cables were about 20m. long because the A/D was in a separate room from the experiment.

amplifies any signal it encounters including noise.

5.4.8 Multiple channel testing

To examine whether cross-talk existed between anemometers on a board, two adjacent anemometer channels on a single board were chosen for a test. The test involved the simultaneous measure of the spectrum in two different jets at two different Reynolds numbers. The coherence function of the two spectra was analyzed to see if there was any relation between the two channels. Zero coherence represents two independent random processes and unity coherence represents 2 linearly correlated signals. Fig. 5.14 shows the coherence function as well as the two original spectra. The coherence function is practically zero (0.02) over the entire range of the spectrum indicating no correlation or cross talk between channels.

5.5 Summary

These tests display the attributes of the Buffalo multi-channel anemometer. The design is optimized to perform many channel measurements with only a few channels of analog to digital conversion. The circuit has been shown to capture the true statistics of the turbulent velocity field when compared to an industry standard anemometer circuit. The noise level is lower in the Buffalo anemometer than in anemometers commercially available and there is no cross-talk between anemometers on a board. The design is well suited for the experiment at hand which requires simultaneous velocity measurements at a large numbers of points and does so at about one tenth the cost of commercial units.

Chapter 6

Preliminary Results

6.1 Introduction

In the first section of this chapter the flow field under investigation is examined. The mean flow field is presented through a series of contour plots and iso-surface renderings. The fluctuating velocity field is also studied in a similar manner. The spectral character of the turbulent velocity field is investigated via a series plots of data at different positions in the mixing layer.

The efficiency of the POD reconstruction is examined by comparing a velocity trace recovered from the hot wire anemometer and that obtained via the POD eigenfunctions and coefficients (v. 2.29). The POD results are also tested through a comparison of spectra calculated from the original velocity field and from the POD's eigenfunctions and coefficients. Comparison with the data of Glauser (1987) will be made throughout this section.

6.2 Numerical Implementation

Before proceeding to the results of the POD, a look at the implementation of the numerical code might be helpful. Typically, in the implementation of the POD, as in Glauser (1987), the kernel of the integral equation, the two point correlation tensor v. eq. 2.32, is formed from the velocity measurements made at each of the points in the field. A tremendous reduction in computational time can be had if instead of working with the two point correlation, the cross spectra between points is used. In this case the instantaneous velocity is first transformed into Fourier space and the two point cross spectrum is formed from the resulting Fourier coefficients by the ensemble averaging the blocks of data to ensure statistical convergence. The cross spectra can then be azimuthally decomposed via eq. 2.17. into azimuthal Fourier modes, as discussed in section 2.4, to form the kernel. The integral eigenvalue equation can then be solved for the eigenfunctions and eigenvalues.

This application of the POD, however, requires the double transformed instantaneous velocity, $\hat{u}_1(r, m, f)$, for the determination of the random coefficients, $\hat{a}_n(m, f)$ (v. eq. 2.33). So it is advantageous to first transform the original velocity in time and azimuthal Fourier modes before forming the cross spectra since it will be necessary to do this later anyway. This reduces the computational time. Also, it is necessary to perform the projection in this manner because the non-uniform azimuthal distribution of probes at the 6 different radii (v. fig. 3.2) precludes a single azimuthal decomposition.

The idea of the technique is to first Fourier transform in time each velocity trace measured at all 138 positions,

$$\hat{u}(r,\theta,f) = F.T.\{u(r,\theta,t)\} = \int_{-\infty}^{\infty} e^{(-i2\pi ft)} u(r,\theta,t) dt$$
 (6.1)

The numerical implementation of the transform is performed with a standard FFT algorithm, in this case the IMSL routine FFTRF. The result is a set of velocity spectra, $\hat{u}_k(r,\theta) = \hat{u}(r,\theta,k\Delta t)$, which are not continuous in frequency but rather discretely evaluated at each of the k frequencies where $f = k\Delta f$ and $\Delta f = 1/T$, (T being the record length = 0.5 sec)

A series of arrays composed of the transformed velocities at each radius were formed, one for each radius, and subsequently transformed into azimuthal modes. This decomposition was performed using a discrete Fourier transform given by,

$$\hat{u}(r,\theta,f) = \sum_{m=0}^{\infty} c(r,m,f) \exp(im\theta)$$
(6.2)

The coefficients of the transform, the azimuthal "modes", are determined using the orthogonality of the Fourier functions,

$$c_k(r,m) = \frac{1}{\pi} \int_{-\pi}^{\pi} \hat{u}_k(r,\theta) \exp(im\theta) d\theta$$
 (6.3)

where m is the azimuthal mode number denoting the wavelength of the particular mode. This equation represents the decomposition of the streamwise velocity Fourier coefficients into azimuthal modes at each of the frequencies. The discrete form of eq. 6.3 which was utilized in the numerical code is given by,

$$c_{l,k}(r) \approx \frac{1}{\pi} \sum_{n=1}^{N_{\theta}} \hat{u}_k(r,\theta) \exp(il(n-1)\Delta\theta)\Delta\theta$$
 (6.4)

where l is the counter representing the discrete azimuthal mode number, N_{θ} is the number of azimuthal positions at which the velocity is measured (v. section 3.4) and $\Delta\theta = 2\pi/N_{\theta}$ is the azimuthal spacing. Substituting in for the azimuthal spacing produces,

$$c_{l,k}(r) \approx \frac{2}{N_{\theta}} \sum_{n=1}^{N_{\theta}} \hat{u}_k(r,\theta) \exp\left[\frac{2\pi i l(n-1)}{N_{\theta}}\right]$$
 (6.5)

The summation given in 6.5 could be solved using a slow discrete summation technique, however it is often advantageous to use the much more efficient FFT algorithms. Typical FFT algorithms reduce the number of computations from N^2 to $N \log N$ where N is the number of points in the transform. The FFT does not quite perform the operations suggested by eq. 6.5 but rather the following,

$$b_m = \sum_{n=1}^{N} s_n \left\{ \cos \left[\frac{2\pi (m-1)(n-1)}{N} \right] - i \sin \left[\frac{2\pi (m-1)(n-1)}{N} \right] \right\}$$
 (6.6)

The two equations can be equated however if l = m - 1 and the FFT coefficients, b_m are scaled by the quantity $2/N_{\theta}$. The IMSL subroutine used for the azimuthal decomposition is FFTCF, which calculates the Fourier coefficients for a complex array, and the above manipulations were performed on the coefficients returned by the routine.

Now that the double Fourier transformed velocity has been formed, the kernel of the POD integral eigenvalue equation is constructed. The procedure is to take the double transformed velocity at each mode number-frequency combination and form an estimator of the kernel in a similar manner as the spectral estimator is utilized in a numerical computation of the velocity spectrum. The details of this derivation are left to appendix A but the result is an ensemble average of the decomposed velocity multiplied by its complex conjugate and normalized by the individual block length, i.e.,

$$W_{1,1}^{E}(r,r',m,f) = \frac{\langle \hat{u}_{l,k}(r)\hat{u}_{l,k}^{*}(r') \rangle}{T}$$
(6.7)

where the E superscript signifies an estimator of the real POD kernel and T is the length of each individual block used in the ensemble average of eq. 6.7. This estimator was then utilized in the numerical approximation to the integral eigenvalue equation as outlined in section 3.2.

6.3 Preliminary Results

6.3.1 Flow Field

Mean and RMS

The velocity measurements made using the probe array described in section 3.4 are presented in this section. There were 300 blocks of 1024 discrete velocity measurements recorded for this experiment. There were 10 blocks of data which were determined to be faulty due to a mismatch between the A/D timing and that of the digital control board (v. section 5.4.3). These 10 blocks of data were excluded in the data processing.

The 290 remaining data blocks were ensemble averaged and integrated over time to obtain estimates of the mean and rms velocities at each of the probe locations. Contours of mean velocity are presented in fig. 6.1 and are found to be circular, confirming that an axisymmetric shear layer has been formed. The mean velocity near the high speed side of the layer is approximately 12 m/s and decreases to about 2 m/s at the low speed side of the layer.

In fig. 6.2 a slice of the mean velocity field is shown. The mean velocity at each point along a line perpendicular to the flow axis has been normalized by the exit velocity ($U_{exit} = 12.5m/s$). The data points in the figure are taken from the average velocity calculated at probe numbers 131, 99, 67, 37, 16, 5, 2, 10, 25, 51, 83, 115 (see fig. 3.2). The plot shows that much of the velocity field in the mixing layer at x/d = 3 is within the bounds of the probe array. The normalized mean velocity is 0.987 at z/d = 0.15 and decreases to 0.200 at z/d = 0.8 ¹. In fig. 6.2 the axial component of

¹The z coordinate is used here to describe the position along the horizontal line through the r=0 coinciding with z=0

Figure 6.1: Mean contours in the axisymmetric mixing layer



98

Figure 6.2: Mean and rms values of the streamwise velocity along a line in the mixing layer. (a) Normalized mean velocity (b) Normalized rms velocity.

the Reynolds stress normalized by the exit velocity, $\sqrt{\overline{u^2}}/U_{exit}$, is presented. A double peak in RMS velocity is shown with a slightly higher peak along the line to the left of the center. These measurements are consistent with a turbulent axisymmetric mixing layer as discussed in Hussein *et al.* (1994) and Glauser *et al.* (1995).

Spectra

The spectral makeup of the velocity field in the mixing layer can be seen in fig. 6.3. The spectra near the high speed side of the mixing layer, $r/d \leq 0.41$ peak away from the origin which is consistent with other researchers (v. Bradshaw et al. (1964) and the references therein). As the mixing layer is traversed radially, the peak in the spectra shifts to the low frequencies as is consistent with the measurements of Bradshaw et al. (1964) and Glauser et al. (1995) and they show at least one full decade of $k^{-5/3}$ range denoting high Reynolds number turbulent flow. Note that the frequency of the preferred mode in the axisymmetric mixing layer corresponds to the peak in the spectra near the high speed side in fig. 6.3 as discussed in Hussain and Zaman (1981) and Hussain (1983). The frequency at which this occurs is approximately 100 Hz which corresponds to a Strouhal number ($St_D = fD/U_{exit}$) of about 0.8.

It is important to note that the spectra presented in fig. 6.3 have been post processed to remove a DC offset that was found to pervade the inner radii measurements. The noise is believed to be a post-anemometer influence caused by some sort of spike initiated by the high current draw of the inner radii anemometers. Since any high frequency disturbances would have been eliminated by the Bessel filters if they had been due to the anemometer, the noise must have come from an instability on the board ground or, more likely the, cable ground ². Since the Fourier transform of a

 $^{^2}$ Since the cables connecting the A/D were triax, a separate ground was available to shield the anemometer output. It is possible that this ground caused the problem.

Figure 6.3: Spectra at each of the 6 radii in the mixing layer

Figure 6.4: Spectra at r/D=.15 for the original and filtered Fourier coefficients

spike is an infinite band DC shift, the spectral levels at all frequencies will have a constant added to them. Note that since the spike is uncorrelated with the velocity it will be filtered out by the POD but, to ensure that this effect is not included in the reconstruction of the original signal it has been filered out of the Fourier coefficients.

The DC offset which was found in the spectra was removed by operating on the frequency transfer of the velocity with a simple digital filter of the form,

$$H = \frac{1}{1 + i\left(\frac{f}{f_o}\right)} \tag{6.8}$$

where $i = \sqrt{-1}$ and $f_o = 200$ the corner frequency. The filter is a simple single-pole which reduces energy in the high frequencies while having little effect on the low ones. The function was used to filter the Fourier coefficients in the determination of the 1-D spectra and in the transforms necessary in the POD. In fig. 6.4, the original and filtered spectra are shown and the effect of the filtering function is obvious. The white noise has been eliminated and the energy containing region of the spectrum is maintained to a sufficient degree. The difference between the whole line integral of the original and filtered spectra (integrated from 2-200 Hz) was about 11%.

The spectra at each of the positions in the mixing layer are presented in figs. 6.5, 6.6 and 6.7. The spectra are presented in individual plots each representing a separate radius in the probe array (v. fig. 3.2). To within experimental error, the spectral nature of the data set conforms to an axisymmetric mixing layer, *i.e.* the distribution of kinetic energy for each frequency at each radius is equal.

6.3.2 POD Decomposition

The effectiveness of the Proper Orthogonal Decomposition at decomposing a field into an optimal set of functions has been shown by many researchers (v. Herzog (1986), Moin and Moser (1989), Ukeiley et al. (1991) among others). In the present analysis the effectiveness of the POD will be illustrated with a plot of a spectra in the mixing layer as determined from the original velocity field and one formed from the first few POD eigenfunctions. The streamwise spectrum in the turbulent field, $S_{11}(f)$, can be recovered from the eigenfunctions in the following manner,

$$S_{11}(r, m, f) = \frac{\langle \hat{u}_1(r, m, f) \hat{u}_1^*(r, m, f) \rangle}{T}$$
(6.9)

where T is the record length. The above equation is the definition of the spectral estimator (v. A.1) but we can substitute in the POD representation of the streamwise

Figure 6.5: Spectra at (a) r/D=0.15 and (b) 0.28 for all azimuthal positions

Figure 6.6: Spectra at (a) r/D=0.41 and (b) 0.54 for all azimuthal positions

Figure 6.7: Spectra at (a) r/D=0.67 and (b) 0.80 for all azimuthal positions

velocity,

$$\hat{u}_1(r, m, f) = \sum_{n=1}^{\infty} a_n(m, f) \phi_1^n(r, m, f)$$
(6.10)

yielding

$$S_{11}(r, m, f) = \frac{\langle \sum_{n} \sum_{n'} a_n a_{n'}^* \phi_1^n \phi_1^{n'*} \rangle}{T}$$
(6.11)

and using the uncorrelated property of the coefficients (eq. 1.32)

$$S_{11}(r, m, f) = \frac{\langle \sum_{n} \lambda_{n} \phi_{1}^{n} \phi_{1}^{n*} \rangle}{T}$$
(6.12)

but since the flow is stationary

$$S_{11}(r, m, f) = \sum_{n} \lambda_n \phi_1^n \phi_1^{n*}$$
(6.13)

This result provides a check on the POD decomposition. A plot of a spectrum calculated in the mixing layer and its POD representation for the first few POD modes is presented in fig. 6.8. As this figure shows, the majority of the energy in the flow is contained in the first POD mode. The second mode is also quite important but does not nearly contain the amount in the first and higher POD modes contain less information. After 5 POD modes, the original spectra is nearly completely recovered. If the spectrum is integrated over frequency, 90% of the area under the spectrum of the original data is covered by the first 3 POD modes. The portion of each POD mode is presented in table 6.1 where the integral of the original signal is 0.210857.

Another interesting check on the POD eigenfunction representation of the velocity field lies in the reconstruction of the instantaneous signal by the POD modes. The velocity field, in this instance, can be recovered using the expansion presented in eq. 2.29. The coefficients, $a_n(m, f)$, in the expansion are obtained via a projection of the POD eigenfunctions onto the instantaneous signal (v. eq. 2.33). The coefficients can

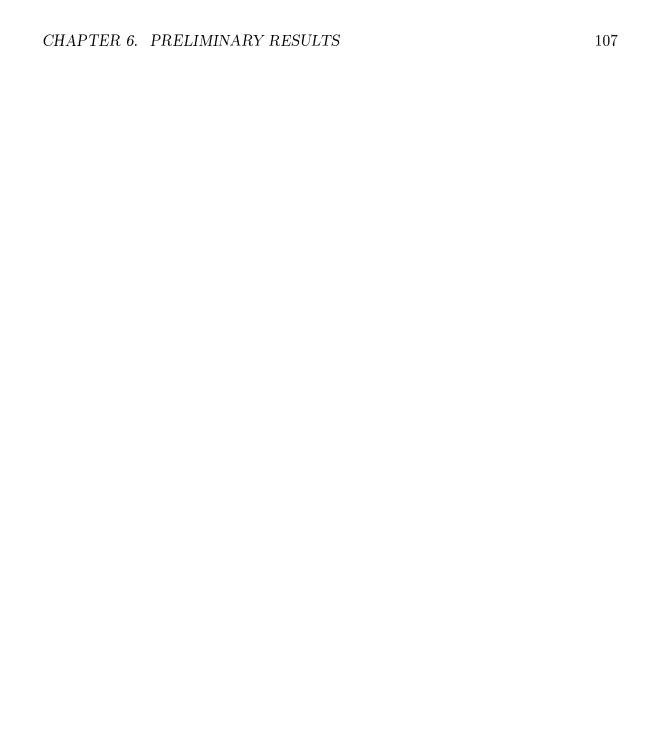


Figure 6.8: Pod reconstruction of spectrum in mixing layer for the first 5 POD modes

	Integral	
POD mode(s)	Value	Percent
1	0.144453	68.5%
1+2	0.174869	82.9%
1+2+3	0.196600	93.2%
1+2+3+4	0.202498	96.0%
1+2+3+4+5	0.210553	99.6%

Table 6.1: Portion of area under spectra contained in the POD modes

then be used to represent the original signal, but in this case only the parts of the signal which are representative of the large scale structure are recovered. This can be seen in fig. 6.9 where a trace of the original velocity is presented along with the reconstructed signal from the first few POD modes. In part (a) of the figure the first PEA is presented ³. As expected the first PEA recovers a large portion of the velocity trace. As more PEA's are added (part (b) combines the first 2 PEA's) more of the signal is recovered. By part (c) nearly all of the trace is recovered.

The ability of the of the first POD mode to represent a large portion of the field is not new to this investigation, but the fact the it is such a tremendous contributing factor is unique. The spectral reconstruction by the first POD mode in fig. 6.8 and the recovery of the velocity trace to such a high degree by the first PEA show the outstanding effectiveness of the first POD in organizing the flow field into a few modes. As we will see later, much of the large scale structure in the flow is contained in the first POD mode and it will be this factor which will allow a unique perspective on the structure of the turbulence in the mixing layer.

³recall a PEA is defined as the product of a coefficient and its corresponding eigenfunction

109

Figure 6.9: Pod reconstruction of instantaneous velocity in mixing layer for (a) first PEA, (b) first 2 PEA's and (c) first 3 PEA's

Chapter 7

Results

7.1 Introduction

This chapter is concerned with the representation of the velocity field as given by the Proper Orthogonal Decomposition. The POD provides an optimal representation of the velocity field; optimal implying that only the minimum number of functions in the transform are necessary to represent the energy of random vector field. In this chapter, the velocity field is reconstructed using various numbers of POD functions to demonstrate the ability of the POD to represent the large scale dynamics of the turbulent velocity field. The dynamics of the structures in the mixing layer are then studied using a reconstruction of the field using only the first POD mode together with various combinations of the azimuthal and temporal Fourier modes.

7.2 POD Velocity Reconstruction

The reconstruction of the double Fourier transformed ¹ velocity field, $\hat{u}_1^{nmf}(r, m, f)$ was shown in chapter 2 to be

$$\hat{u}_1^{nmf}(r, m, f) = \sum_n a_n(m, f)\phi_1^n(r, m, f)$$
(7.1)

where the coefficients, $a_n(m, f)$ are in turn given by

$$a_n(m,f) = \int \hat{u}_1^{nmf}(r,m,f)\phi_1^{n*}(r,m,f)rdr$$
 (7.2)

The most interesting form of 7.1, at least from a visual standpoint, is the inverse Fourier transform in time of \hat{u}_1^{nmf} ,

$$\hat{u}_1^{nm}(r, m, t) = \int e^{i2\pi f t} \hat{u}_1^{nmf}(r, m, f) df$$
(7.3)

since it is the time dependent contribution of from each n-m pair. This quantity and various partial sums (i.e. N=1,2,3... and/or m=0,1,2,3...) will be examined in detail, along with its inverse transform in the azimuthal direction, $u^n(r\theta,t)$, given by,

$$u_1^n(r,\theta,t) = \sum_{n=1}^N \sum_{m=0}^\infty e^{-im(\theta'-\theta)} u_1^{nm}(r,m,t)$$
 (7.4)

7.3 Numerical Implementation

The numerical implementation of equation 7.2 was performed using Simpson's 1/3 rule and eq. 7.1 with a straightforward sum. The details on the use of Simpson's 1/3 rule for this experiment are provided in section 3.2. The velocity obtained from the PEA's, eq. 7.1, is inverse transformed in azimuthal modes and time to obtain

¹In time and azimuthal modes

the velocity reconstruction of each channel in the measurement grid (v. fig. 3.2) for whichever POD modes and azimuthal modes desired. For instance, the reconstructed velocity field could include only the first PEA or only 1 or 2 azimuthal modes or any combination of them. It is easy to accomplish this by simply setting the appropriate Fourier coefficients in \hat{u}_1^{nm} equal to zero. Thus, any imaginable reconstruction of the velocity field is possible.

7.4 Energy Distribution in Mixing Layer

In the previous chapter, it was determined that the first POD mode made a significant contribution to the spectra in the mixing layer. In this section, a more quantitative measure of the importance of the first POD mode is presented. Recall from chapter 2 that the total kinetic energy in the flow, as recovered in the POD modes, is equal to the sum of the POD eigenvalues, $\lambda_n(m, f)$ (v. eq. 2.9). This fact provides a useful way to study the distribution of energy in the flow for the different POD modes. Also, since the eigenvalues are already azimuthal mode number, m, dependent, it is useful to look at the distribution of energy for each azimuthal mode comprising each eigenvalue. If the energy in each azimuthal mode for each POD mode is normalized by the total energy in the flow, the parameter, ξ can be determined, where

$$\xi = \frac{\sum_{f} \lambda^{n}(m, f)}{\sum_{n} \sum_{f} \sum_{f} \lambda^{n}(m, f)}.$$
(7.5)

The results of this distribution are presented in figure 7.1. The first POD mode is found to contain nearly 67% of the kinetic energy in the flow. This agrees well with the value of 68% which was determined previously at a single position in the mixing layer and again stresses the effectiveness of the POD. The interesting feature

Figure 7.1: Azimuthal-mode energy distribution in the first 5 POD eigenvalues

of fig. 7.1 is the energy content at each azimuthal mode within each POD mode. In the first eigenvalue, there is a definite predominance of the zero azimuthal mode. It is interesting, however, that the next largest azimuthal mode is m=4 with modes 3, 5 and 6 not much smaller. Also interesting is that this trend continues for all of the eigenvalues. This would tend to imply that although the zero, or ring, mode is dominant, it is also important to consider the effect of these higher azimuthal modes. For instance, nearly 15% of the total energy in the flow is found in mode 0 of the first eigenvalue but almost 25% is found in modes 3, 4, 5 and 6. So 40% of the kinetic energy in the flow is found in those 5 modes. The POD has done an excellent job at reducing a nearly infinite dimensional problem to one involving only 5 parameters. The results of this distribution will be used in the next section to investigate the spatial structure in the mixing layer.

The eigenspectra, $\lambda^n(m, f)$, are presented as a function of frequency for the first 10 azimuthal modes in figs. 7.2 - 7.6. They show the progression of the energy containing region of the spectra to the low frequencies for higher azimuthal modes. This suggests one of two things; the dominant higher azimuthal modes occur in the outer portion mixing layer (m=3,4,5,6) (v. Glauser (1987)) where the convection velocity is lower so they appear at a lower frequency, or azimuthal mode number aliasing has appeared to make the frequency distribution shift. Now since a good deal of the preparation in this experiment focused on the elimination of azimuthal aliasing (v. chapter 3), the latter is not likely so the higher azimuthal modes can indeed be associated with only the outside of the flow as suggested by Glauser et al. (1995).

If the interaction between the inner and outer radii behaves like a 2 ring leap frog effect the dominant modes at the inner radii would tend to slow the convection of the modes at the outer radii. This is just like the interaction between two rings where

m	λ^1	λ^2	λ^3	λ^4	λ^5
0	0.14699E+00	0.20192E-01	0.10220E-01	0.53688E-02	0.31942E-02
1	0.34754E-01	0.13498E-01	0.70824E-02	0.42293E-02	0.26098E-02
2	0.44416E-01	0.13615E-01	0.84099E-02	0.50862E-02	0.35658E-02
3	0.64448E-01	0.20748E-01	0.12471E-01	0.68928E-02	0.27021E-02
4	0.74914E-01	0.24522E-01	0.12653E-01	0.67353E-02	0.26648E-02
5	0.62810E-01	0.13140E-01	0.80876E-02	0.43501E-02	0.23953E-02
6	0.56385E-01	0.12881E-01	0.69537E-02	0.24473E-02	0.57095E-08
7	0.45118E-01	0.11649E-01	0.63502E-02	0.22333E-02	0.46394E-08
8	0.34995E - 01	0.92133E-02	0.47121E-02	0.20356E-02	0.40232E-08
9	0.25998E-01	0.84217E-02	0.43730E-02	0.19125E-02	0.25930E-08
10	0.19795E-01	0.64195E-02	0.27688E-02	0.15937E-02	0.19117E-08
11	0.17427E-01	0.60642E-02	0.24923E-02	0.14397E-02	0.17019E-08
12	0.14022E - 01	0.50064E-02	0.15172E-02	0.14904E - 08	0.74520E-09
13	0.11901E - 01	0.43410E - 02	0.14233E-02	0.12537E-08	0.62686E-09
14	0.89735E-02	0.38086E-02	0.13779E-02	0.95364E-09	0.47682E-09
15	0.64362E-02	0.34234E-02	0.13454E-02	0.67696E-09	0.33848E - 09
total	0.66938E+00	0.17695E+00	0.92238E-01	0.44325E-01	0.17132E-01

Table 7.1: Kinetic energy distributed in azimuthal modes for each POD mode

Figure 7.2: Eigenspectra for the first 3 POD modes and for azimuthal modes: (a) m=0 and (b) m=1

Figure 7.3: Eigenspectra for the first 3 POD modes and for azimuthal modes: (a) m=2 and (b) m=3

Figure 7.4: Eigenspectra for the first 3 POD modes and for azimuthal modes: (a) m=4 and (b) m=5 $\,$

Figure 7.5: Eigenspectra for the first 3 POD modes and for azimuthal modes: (a) m=6 and (b) m=7

Figure 7.6: Eigenspectra for the first 3 POD modes and for azimuthal modes: (a) m=8 and (b) m=9 $\,$

one is blown through another created just before it. The second ring will impede the motion of the first as it projects itself through the inside of the first, thereby slowing the outside ring and causing it to become unstable. This type of interaction could indeed cause the shift in the peak of the eigenspectra of figs. 7.2- 7.6. To be sure of this, the temporal dynamics of the POD modes, contained in the POD coefficients, must be known because they provide the timing of the PEAs', *i.e.* they determine when each PEA increases in value (turns on) or decreases. This synchronization of events in the mixing layer is contained in the POD coefficients.

7.5 Temporal Resolution of Spatial Structures

The goal of this experiment was to gain an understanding of the dynamics of the large scale turbulent structures in the axisymmetric mixing layer and compare and contrast two competing models of the structure dynamics. The most effective way to do this is to visualize the flow field at each instant in time and view the structures which are there. In the present experiment, the entire velocity field is captured at every $\Delta t = 0.5 \text{ sec} \div 1024 \text{ samples} = 4.88281 \text{x} 10^{-4} \text{sec}$. The integral scale in the flow can be estimated to be

$$\mathcal{L} = \frac{l}{U_{conv}} \tag{7.6}$$

where l is a representative scale of the turbulent structures and U_{conv} the convection velocity of this scale. If the large scales in the mixing layer are assumed on order of the jet diameter, D, and the longitudinal integral scale grows at a rate proportional to 0.1x in the streamwise, x, direction (Khwaja, 1981) then at an x/D = 3

$$\mathcal{L} = \frac{0.3D}{0.6U_{cl}},\tag{7.7}$$

where the convection velocity is assumed to be 60% of the centerline velocity, U_{cl} (Khwaja, 1981). For an exit velocity of 12.5 m/s and a jet diameter of 0.098 m, the integral scale is 0.004 sec. In the present experiment, this means there are about 8 time samples per integral scale. Over the entire 1/2 second record there are approximately 125 integral scales and consequently about 125 large scale eddies.

7.5.1 Animation

The magnitude of the streamwise velocity at each of the 138 channels of anemometry is known at x/D=3 for each time step, $t=t_n\Delta t^{-2}$. Each of the n "slice's" of the flow is then imported into a graphics package (pv-wave) which grids the data onto a 40x40 grid. Each grid point can then be colored according to the value of the velocity. If consecutive time steps are processed in this manner, an animation showing the evolution of the velocity field is produced; in essence, a high speed video of the streamwise velocity field at x/D=3. The animation process can also be performed on the velocity signals reconstructed from the PEA's (v. eq. 7.3). The velocity field recovered by the POD can then be compared with the original field to see how the energetic structures in the flow behave.

A number of time steps (50 typically) have been selected from a section of one of the blocks of data and plotted as discussed above. Since the author could not get a CD-ROM to send with each copy of the dissertation he has decided to place the video images, in mpeg form, on the internet at the following address: http://www.eng.buffalo.edu/research.html. Anyone who wishes to see the animation in color can download the mpeg's and play them on their system. In the following analysis the data from the 138 anemometer channels will be presented in single image

The absolute time for each block of data will be indexed by t_n where $1 < t_n < 1024$.

form. However, the true power of the presentation is in the full motion animation. The author has chosen a few select images which best capture the important events in the life cycle of the eddies in the flow.

7.6 Structure in the Axisymmetric Mixing Layer

The difficulty in visualizing the structure in the flow is the tremendous number of scales present. The large scale structure is often masked by short duration pulses. However, we have already seen how effective the POD is at organizing energy into a few or even one mode so it is natural to select this method in representing the field in a visual manner. In effect, the POD has objectively filtered out the small scale structure which tends to cloud the view of the large scales. To see the POD's effectiveness, look at fig. 7.7 which shows a slice of the streamwise velocity in the mixing layer at x/D = 3 from the original velocity data at $t_n = 524$. Each color on the plot corresponds to a particular value of the velocity magnitude with the lighter images (the bright yellow) indicating the highest velocity (approximately 12 m/s). The dark areas, near the outside of the image represent low velocities (the blue is about 2 m/s).

As this image shows, there is a quite complicated motion at this particular instant in the flows evolution. The middle of the mixing layer exhibits a complicated, multiple mode shape with almost ejection-like events at 8 o'clock and 1 o'clock. It is difficult in this case to determine what events in this figure are short duration events and which control the main features of the turbulence. However, if the same time step is presented with the velocity recovered from the PEA's, a more ordered pattern is exhibited. Figure 7.8 shows the same time step with the PEA velocity using only

the first mode (i.e. n = 1 in 7.3). The structure exhibited in this figure is similar to that in fig. 7.7; the lobes seen at 1 o'clock and 8 o'clock are still evident as well as one at 5 o'clock but many of the smaller events have been filtered out by the POD. Undoubtedly, these events were not significant contributing factors to the kinetic energy of the flow. The POD has filtered them out and left us with a substantially more ordered view of the field.

The flow field can be broken into even fewer parts if the results of section 7.4 are utilized. The POD eigenvalue decomposition in this section indicated that much of the energy in the first POD mode was contained in azimuthal modes 0, 1, 3, 4, and 5. If these modes can be included and the others left out, a further filtering of the small scale structure can be accomplished. To insure that the features of the flow are not lost, a comparison between the original velocity and the PEA reconstruction can be performed.

The original velocity color contour plot at $t_n = 584$ is presented in fig 7.9. The PEA velocity from the first POD mode and including all azimuthal modes is presented in fig. 7.10. Again, the salient features of the flow are recovered without the small scales obscuring the underlying structure. If only azimuthal modes 0, 1, 3, 4 and 5 are included in the PEA reconstruction the field is even further reduced in complexity but the salient features of the flow are still evident in fig. 7.11. Also, it is important to note that even with these few azimuthal modes, the multi-lobed structure in the outer portion of the mixing layer dominates this region.

This process of reducing the information in the reconstruction can obviously continue until all that remains is the mean velocity. However, the view afforded to us by the POD has shown that instead of an infinitely dimensional problem, we can successfully describe the large scale features of the flow with only 5 parameters. This

Figure 7.7: Color contour plot of velocity field - Original velocity, $t_n=524$

Figure 7.8: Color contour plot of velocity field - PEA Reconstruction, $t_n=524$

Figure 7.9: Color contour plot of velocity field - Original Velocity, $t_n=584$

Figure 7.10: Color contour plot of velocity field - PEA reconstruction, first POD mode and all azimuthal modes included, $t_n=584$

Figure 7.11: Color contour plot of velocity field - PEA reconstruction, first POD mode and azimuthal modes 0,1,3,4,5, $t_n=584\,$

trying to model the dynamics of the turbulent structures in jet mixing layers (v. Miller et al. (1995), Grinstein et al. (1986) and the references therein) and for those interested in the structure of the turbulence in the mixing layer.

7.6.1 Single Azimuthal Mode Representation

In the preceding figures it is evident that the dominant azimuthal mode in the inner portion of the mixing layer is the zeroeth mode. Therefore, a series of plots were constructed which showed the color contour of the field from the first PEA and only azimuthal mode zero. The structure in the flow is obviously being forced at this point into a circular mode but what can be gleaned from this is the temporal dynamics between the inner and outer portion of the mixing layer. In fig. 7.12 the result of this reconstruction of the field is presented using a slightly different color scheme ³. It is important to study the innermost ring (light purple) and the second most outer ring (light yellow). In this figure the inner ring is small and the outer ring quite large. In the next figure 7.13, the inner ring is seen to grow in size while the outer ring lessens in its extent. If the next step in the series was presented it would look very similar to the structure in fig. 7.12 which suggests that a repeatable pattern of phase lag exists between the inner and outer portion of the mixing layer. Finally, it is evident from the results of this section and those of sec. 7.6 that a ring like structure exists in the inner portion of the mixing layer and a multi-lobed, out of phase with the inner radius, structure exists at the outer portion of the layer. These two structures are also seen to interact in a repeatable pattern of phase-lagged interaction.

³This color scheme was chosen because it better highlighted the interaction between the inner and outer portions of the mixing layer.

Figure 7.12: Color contour plot of velocity field - PEA reconstruction, first POD mode and azimuthal mode 0 included, $t_n=506$

Figure 7.13: Color contour plot of velocity field - PEA reconstruction, first POD mode and azimuthal mode 0 included, $t_n=514$

7.7 Four Azimuthal Mode Representation

To better bring out the structure in the layer the previous set of plots have reconstructed the velocity field using fewer and fewer azimuthal modes, for the first PEA, in order to filter out the small scale structure and reveal the hidden large scale structure within. In this way we have been able to summize that two ring-structures, one circular near the potential core and one multi-lobed near the outside of the layer, are formed due to the instabilities arising from the turbulence production near the edge of the layer. To show with convincing evidence that the two ring structure exists, another series of plots is presented. These plots present the velocity reconstruction from the first PEA using azimuthal modes 0, 4, 5, 6. The difference between this and previous presentations is that the mean velocity is now excluded from the plots so that the structure which has been hidden due to the small variance and large mean velocity can be revealed. The results of this reconstruction are presented in figs. 7.14, 7.15 and 7.16.

The velocities represented by colors below the square shading plane in fig. 7.14 are negative, indicating a value less than the mean, while those above the plane are positive, or a fluctuation larger than the mean. The time index for this figure is $t_n = 584$. The striking aspect of the image is the multi-lobed structure near the outside of the mixing layer and the large "negative" velocities near the center. The same imaging, applied to a time step slightly after this one $(t_n = 589)$, illuminates a highly correlated ring structure piercing the cutting plane⁴. This ring then breaks down and another multi-lobed structure appears near the outside of the mixing layer, as seen in figure 7.16 where in this figure $t_n = 593$. In this figure, the potential

⁴The ring is not quite circular at its peak because of the gridding routine used in pv-wave.

Figure 7.14: Color contour plot of velocity field: NO MEAN VELOCITY, first PEA and azimuthal modes 0.4.5.6 included. $t_n=584$

Figure 7.15: Color contour plot of velocity field: NO MEAN VELOCITY, first PEA and azimuthal modes 0.4.5.6 included. $t_n=589$

Figure 7.16: Color contour plot of velocity field: NO MEAN VELOCITY, first PEA and azimuthal modes 0,4,5,6. $t_n=593$

core ring of fig. 7.15 has passed through the measurement plane and another multilobed structure has arrived to dominate the layer. This sequence, consisting of a ring passing through the measurement plane at the potential core followed immediately by a multi-lobed structure, is found, in a repeatable pattern, throughout the entire time history of the data. This indicates that the event is not unique and that it must be instigated by the flow field.

The velocity pattern in fig. 7.15 shows, without question, that the dominant turbulent structure in the layer near the potential core is a circular ring. The sequence of events which surrounds this figure provides the most striking evidence that two distinct structures interact in the mixing layer. Although, it is hard to say, unequivocally, what the order of the interaction is, *i.e.* does the structure near the outside of the layer lag or lead the highly correlated inner ring. The sequencing of the inner and outer structures will be examined further in future investigations of the data set.

Chapter 8

Conclusions

8.1 Turbulent Production Mechanism

At the outset of this thesis, two competing models for the production of turbulence in the axisymmetric mixing layer were presented. One model from Hussain (1986) suggests that the turbulence production mechanism in the axisymmtric mixing layer is initiated by a cut-and-connect process. In this process, a single vortex ring is shed from the jet nozzle, grows as it is convected with the flow, and becomes unstable. At this point the single, multi-lobed vortex cuts and reconnects to form a circular, center ring and many outer rings (v. fig. 1.1). The other model (Glauser (1987)) suggests that the mechanism is more like two inviscid rings, leapfrogging through one another. The outside ring, driven unstable by the trailing inner ring, forms an unstable, multilobed structure near the outer edge of the mixing layer. Eventually, the outer ring breaks apart into a multitude of small vortex rings which in turn feed energy into the dissipation scales in the so called energy cascade. The instability of the outer ring is driven by the stretching due to the induced velocity field from the

following, inner ring.

From the measurements presented in the previous sections it seems clear that the two vortex ring model of Glauser (1987) more closely matches the structure interaction seen in the velocity reconstruction data of secs. 7.6 and 7.6.1. It becomes even more evident when the animation of the flow field is played and the temporal dynamics of the structures can be seen. In the video, and this can also be seen in figs. 7.12 and 7.13, the pulsing of the inner and outer rings in the mixing layer is evident and this seems like unmistakable evidence for the existence of two vortex rings interacting in the mixing layer. Further evidence is apparent in section 7.7 in which a ring like structure is observed near the potential core with multi-lobed structures appearing just before and after the ring in our temporal reconstruction of the velocity field.

Therefore, the vortex ring interaction, as suggested by Glauser (1987), can be found consistent with the data and the following conclusions can be drawn:

- The shifting of energy toward the lower frequencies in the higher azimuthal modes of the POD eigenspectra (v. sec. 7.4) implies that the structures associated with these azimuthal modes must be convecting at a speed less than the mean convection velocity in the layer. This implies that the structure in the outside of the layer is multi-lobed.
- The ring-like behavior of the field in the outside portion of the mixing layer (as shown in the PEA reconstruction of fig. 7.8), suggests that a single, multi-lobed structure exists in near the outside portion of the layer.
- Finally, the distinctive interaction between the ring-like structure in the inner portion of the mixing layer and the multi-lobed one in the outer layer, v. sec. 7.7, would suggest that the two structures interact and, based on these facts,

the leap frog effect would explain this interaction.

8.2 Recommendation for Further Study

It should be obvious that the flow visualization alone can not describe all of the interactions of the structures in the mixing layer. Therefore, the data recovered in the experimental aspect of this study can be used to develop more sophisticated techniques for recovering analytical or "hard" data on the existence of the 2 ring structure in the mixing layer. In particular, conditional sampling or wavelet techniques based on the PEA reconstruction can be performed to better extract patterns in the instantaneous signals. Also, further work on the flow visualization can be employed to extract other structure in the layer which is not seen using the modal reconstruction presented. Finally, investigation of the instantaneous coefficients produced by the POD will produce statistical characterization of the structures described by the POD eigenfunctions.

The data set recovered in this experiment is unique. A simultaneous measure of the streamwise velocity field at 138 positions is known at x/D = 3, and the avenues for future investigation seem endless.

Bibliography

Baker, C.T.H. (1977). The Numerical Treatment of Integral Equations. Clarendon Press, Oxford.

Batchelor, G. K. (1953). Homogeneous Turbulence. Cambride University Press.

Bradshaw, P., Ferriss, D.H., and Johnson, R.F. (1964). Turbulence in the noise producing region of a circular jet. *Journal of Fluid Mechanics* **19**, 591–625.

Champagne, F.H., Sleicher, C.A., and Wehrmann, O.H. (1967). Turbulence measurements with inclined hot wires, part 1. *Journal of Fluid Mechanics* 28, 153–175.

Citriniti, J.H., Taulbee, K.D., Woodward, S.H., and George, W.K. (1994). Design of multiple channel hot wire anemometers. In *Fluid Measurement and Instrumentation* 1994, pages 67–73, ASME FED-Vol. 183.

Corrsin, S. (1963). *Handbuch Der Physik*, volume VII/2, chapter Turbulence: Experimental Methods, pages 525–590.

Freymuth, P. (1977). Frequency response and electronic testing for constant temperature hot-wire anemometers. *Journal of Physics E*, 10, 705–710.

George, W.K., Beuther, P.D., and Lumley, J.L. (1978). Processing of random signals. pages 757–800.

BIBLIOGRAPHY 142

George, W.K., Beuther, P.D., and Shabbir, A. (1987). Polynomial calibrations for hot wires in thermally varying flows. In Stock, D., editor, *ASME Symposium on Thermal Anemometry*, Cincinnati, Ohio.

George, W.K. (1988). Insight into the dynamics of coherent structures from a proper orthogonal decomposition. In *Symposium on Near Wall Turbulence*, Dubrovnik, Yugoslavia.

Glauser, M.N. and George, William K. (1992). Application of multipoint mesurements for flow characterization. *Experimental Thermal and Fluid Science* 5, 617–632.

Glauser, M.N., Zheng, X., and Doering, C. (1992). A low-dimensional dynamical systems description of the axisymmetric mixing layer. *Clarkson University Report MAE-427*.

Glauser, M.N., Zheng, X., and George, William K. (1995). An analysis of the turbulent axisymmetric jet mixing layer utilizing the proper orthogonal decomposition.

Journal of Fluid Mechanics, Submitted for Publication.

Glauser, M.N. (1987), Coherent Structures in the Axisymmetric Turbulent Jet Mixing Layer. PhD thesis, State University of New York at Buffalo.

Grinstein, F.F., Boris, J.P., and Griffin, O.W. (1986). direct numerical simulations of axisymmetric jets. *AIAA Journal* **25**, 92.

Hardin, J. C. (1986). *Introduction to Time Series Analysis*. NASA Reference Publication 1145.

Helland, K. N., Atta, C. W. Van, and Stegen, G. R. (1977). Spectral energy transfer in high reynolds number turbulence. *Journal of Fluid Mechanics* **70**, 337–359.

BIBLIOGRAPHY 143

Herzog, S. (1986), The large scale structure in the near-wall region of turbulent pipe flow. PhD thesis, Cornell University.

Hussain, A.K.M.F. and Zaman, K.B.M.Q. (1981). Vortex pairing in a circular jet under controlled excitation. part 2. coherent structure dynamics. *Journal of Fluid Mechanics* **101**, 492.

Hussain, A.K.M.F. (1983). Coherent structures - reality and myth. *Physics of Fluids* **26**, 2816.

Hussain, A.K.M.F. (1986). Coherent structures and turbulence. *Journal of Fluid Mechanics* **173**, 303.

Hussein, H.J., Capp, S.P., and George, W.K. (1994). Velocity measurements in a high-reynolds-number, moment conserving, axisymmetric, turbulent jet. *Journal of Fluid Mechanics* **258**, 31–75.

Khwaja, Muhammed S.S. (1981), Investigation of the turbulent axisymmetric jet mixing layer. Master's thesis, State University of New York at Buffalo.

Lighthill, M.J. (1956). An Introduction to Fourier Analysis and Generalized Functions. Cambridge University Press.

Lumley, J. L. (1970). Stochastic Tools in Turbulence. Academic Press.

Miller, R.S., Madnia, C.K., and Givi, P. (1995). Numerical simulation of non-circular jets. *Computers and fluids* **24**, 1–25.

Moin, P. and Moser, R.D. (1989). Characteristic-eddy decomposition of turbulence in a channel. *Journal of Fluid Mechanics* **200**, 471–509.

BIBLIOGRAPHY 144

Oppenheim, A.V. and Willsky, A.S. (1983). Signals and Systems. Prentice Hall, Englewood Cliffs, New Jersey.

Pao, Y. H. (1965). Structure of turbulent velocity and scalar fields at large wave numbers. *Physics of Fluids* 8, 11063–1075.

Perry, A.E. (1982). Hot Wire Anemometry. Clarendon Press, Oxford.

Sreenivasan, K.R. (1984). The azimuthal correlation of velocity and temperature fluctuations in an axisymmetric jet. *Physics of Fluids* 27.

Tan-atichat, J. and George, W.K. (1985). *Handbook of Fluids and Fluid Machinery*, chapter Use of Computers in Data Acquisition. John Wiley Sons Inc.

Tennekes, H. and Lumley, J.L. (1972). A First Course in Turbulence. The MIT Press, Cambridge.

Townsend, A.A. (1956). The Structure of Turbulent Shear Flow. Cambridge University Press, Cambridge.

Ukeiley, L., Wick, D., and Glauser, M. (1991). Coherent structure identification in a lobed mixer. ASME, $Paper\ 91$ -GT-397.

von Karmen, T. (1948). Progress in the statistical theory of turbulence. In *Pro. Nat. Acad. Sci. USA Vol. 34*, pages 530–539.

Wyngaard, J. C. (1968). Measurement of small-scale turbulence with hot wires.

Journal of Scientific Instruments 1, 1105–1108.

Appendix A

Kernel Formulation

The kernel of the POD integral eigenvalue equation is given by 2.32,

$$W_{1,1}(r,r',m,f) = FT_m\{FT_t\{R_{i,j}(r,r',\theta-\theta',t-t')\}\}$$
(A.1)

where FT represents the Fourier transform and the subscripts denote the azimuthal mode number (m) and temporal (t) versions. Typically, the kernel is formed from the process described in A.1 *i.e.* the correlation tensor is formed by first transforming the velocity measurements in time, forming the kernel and then transforming the kernel in the azimuthal direction. The kernel for this application can not be formed in this manner because of the unequal spacing in the azimuthal direction. So a new method had to be established.

If the streamwise velocity were to be Fourier transformed in time and the azimuthal direction, an estimator for the POD could be derived. This process is outlined below and follows the form of the general spectral estimator common in real data analysis (George et al., 1978).

A.1 Spectral analysis

A real data set, say the velocity vector u(t), can be represented in Fourier space via the transform

$$u(t) = \int_{-\infty}^{\infty} \hat{u}(f)e^{(i2\pi ft)}dt$$
(A.2)

where i is $\sqrt{-1}$. Another quantity of interest is the correlation of the velocity $(R_{i,j}(\vec{x}, \vec{x}', t, t') = \langle u_i(\vec{x}, t)u_j^*(\vec{x}', t') \rangle)$. If eq. A.2 is substituted into this definition the result is,

$$R_{i,j}(\vec{x}, \vec{x}', t, t') = \int_{-\infty}^{\infty} \int_{-\infty}^{\infty} <\hat{u}_i(\vec{x}, f) \hat{u}_j^*(\vec{x}', f') > e^{(i2\pi(ft - f't')} df df'$$
 (A.3)

If the random field is stationary, the correlation no longer is a function of t and t' but only their difference, $\tau = t' - t$. The left hand side of eq. A.3 is no longer an explicit function of time and therefore neither must the right hand side. If the right hand side is written in terms of a delta function,

$$\hat{u}_i(\vec{x}, f)\hat{u}_j^*(\vec{x}', f') = S_{i,j}(\vec{x}, \vec{x}', f)\delta(f' - f)$$
(A.4)

then the conflict in eq. A.3 can be cleared. This implies that the correlation tensor and the spectrum of a random vector field are a Fourier transform pair,

$$R_{i,j}(\vec{x}, \vec{x}', \tau) = \int_{-\infty}^{\infty} S_{i,j}(\vec{x}, \vec{x}', f) e^{(i2\pi f\tau)} df$$
 (A.5)

In a set of real data the vector field is never known at all values of the independent variables so a finite length transform must be defined. In the case of the spectrum the result is,

$$S_{i,j}(\vec{x}, \vec{x}', f) = \lim_{T \to \infty} \int_{-T/2}^{+T/2} R_{i,j}(\vec{x}, \vec{x}', \tau) e^{(-i2\pi f \tau)} d\tau$$
(A.6)

where T is the record length of the data. The convolution property of Fourier transforms (Hardin, 1986) is applied to A.6 after a change of variables and the resulting equation is,

$$S_{i,j}(\vec{x}, \vec{x}', f) = \lim_{T \to \infty} \int_{-T/2}^{+T/2} \left[1 - \frac{\tau}{T} \right] R_{i,j}(\vec{x}, \vec{x}', \tau) e^{(-i2\pi f\tau)} d\tau \tag{A.7}$$

where a biasing window has been formed due to the finite length of the transform. The infinite limit in eq. A.18 prohibits evaluation of the spectrum but the equation suggests a form of a spectral estimator (George *et al.*, 1978),

$$S_{i,j}^{T}(\vec{x}, \vec{x}', f) = \frac{\langle \hat{u}_{i}(\vec{x}, f) \hat{u}_{j}^{*}(\vec{x}', f') \rangle}{T} = \int_{-T/2}^{+T/2} \left[1 - \frac{\tau}{T} \right] R_{i,j}(\vec{x}, \vec{x}', \tau) e^{(-i2\pi f\tau)} d\tau \quad (A.8)$$

where the T superscript signifies that term is an estimator based on the finite record length and the angle brackets represent ensemble averaging. The estimator of the spectrum given in eq. A.8 will approach the true spectrum as long as the record length, T, is long enough 1 .

The numerical discretization of the Forier transform is implemented via a Discrete Fourier Transform (DFT) of the form,

$$X^{T}(f) \approx \frac{\Delta t}{\sum_{n=0}^{N-1}} X(n\Delta t) e^{(-i2\pi f n\Delta t)}$$
(A.9)

where $\Delta t = T/(N-1)$. The evaluation of eq. A.9 is typically performed using the Fast Fourier Transform (FFT) which is an efficient representation of the DFT. The FFT gains a computational advantage because it splits the calculation into two parts as long as N is not a prime integer. This allows a reduction in the number of mathematical computations from N^2 for a direct evaluation of A.9 to approximately $N \log N$ depending on the number of points in the original data set.

As T gets larger the biasing window $(1 - \tau/T)$ approaches unity

A.2 POD kernel Formulation

A derivation similar to that above can be developed to find an estimator for the POD kernel $W_{1,1}(r, r', m, f)$. If the estimator is assumed to take the form,

$$W_{1,1}(r,r',m,f) = \frac{\langle \hat{u}_1(r,m,f)\hat{u}_1^*(r',m,f) \rangle}{T}$$
(A.10)

then we need only show that this approaches the true kernel as the record length increases.

The double transformed velocities in A.10 (over frequency and azimuthal mode number) are given as,

$$\hat{u}_1(r, m, f) = \sum_{m=-N/2}^{N/2} \int_{-T/2}^{T/2} e^{-i(2\pi f t + m\theta)} u(r, \theta, t) dt$$
(A.11)

where m is the azimuthal Fourier mode number, N is the number of azimuthal modes and \hat{u} is the transformed velocity. The estimator for the POD kernel then becomes,

$$\langle \hat{u}_{1}(r, m, f) \hat{u}_{1}^{*}(r', m, f) \rangle = \sum_{m=-N/2}^{N/2} \sum_{m'=-N/2}^{N/2} \int_{-T/2}^{T/2} \int_{-T/2}^{T/2} e^{-i2\pi(ft - f't')} e^{-i(m\theta - m'\theta')} B(r, r', \theta, \theta', t, t') dt dt'$$
(A.12)

where $B(r, r', \theta, \theta', t, t') = \langle \hat{u}_1(r, \theta, t) \hat{u}_1^*(r', m, f) \rangle$ is the correlation tensor. Rewriting A.12 produces,

$$\langle \hat{u}_{1}(r, m, f) \hat{u}_{1}^{*}(r', m, f) \rangle = \sum_{m=-N/2}^{N/2} \sum_{m'=-N/2}^{N/2} e^{-i(m\theta - m'\theta')} \int_{-T/2}^{T/2} \int_{-T/2}^{T/2} e^{-i2\pi(ft - f't')} B(r, r', \theta, \theta', t, t') dt dt'$$
(A.13)

For homogeneous variables in θ and t the term in square brackets of eq. A.13 becomes (after a change of variables $\xi = \theta - \theta'$ and $\tau = t - t'$ and a mapping of coordinate systems),

$$= \frac{1}{2} \int_{-\tau - T}^{\tau + T} e^{-i\pi x(f - f')} B(r, r', \xi, \tau) dx + \frac{1}{2} \int_{\tau - T}^{-\tau + T} e^{-i\pi x(f - f')} B(r, r', \xi, \tau) dx \qquad (A.14)$$

and using the symmetry of the autocorrelation tensor, $B(r, r', \xi, \tau) = B(r, r', \xi, -\tau)$ one obtains,

$$= B(r, r', \xi, \tau) \int_{-\tau - T}^{\tau + T} e^{-i\pi x(f - f')} dx$$
 (A.15)

which can be integrated. The final result is,

$$= \sum_{m=-N/2}^{N/2} \sum_{m'=-N/2}^{N/2} e^{-i(m\theta-m'\theta')} \int_{-T}^{T} e^{-i\pi\tau(f+f')} B(r, r', \xi, \tau) \left\{ \frac{1}{i\pi(f-f')} \left(e^{-i\pi(f-f')(T+\tau)} - e^{i\pi(f-f')(T+\tau)} \right) \right\} d\tau$$
(A.16)

The term in the parentheses of eq. A.16 is the Euler formula for $\sin x$ and its Taylor expansion produces,

$$\langle \hat{u}_{1}(r, m, f) \hat{u}_{1}^{*}(r', m, f) \rangle = \sum_{m=-N/2}^{N/2} \sum_{m'=-N/2}^{N/2} e^{-i(m\theta - m'\theta')} \int_{-T}^{T} e^{-i\pi\tau(f + f')} B(r, r', \xi, \tau) T\left(1 + \frac{\tau}{T}\right) d\tau$$
(A.17)

The interest here is on single point statistics so as $m \to m'$ and $\theta \to \theta'$ eq. A.17 becomes,

$$<\hat{u}_1(r, m, f)\hat{u}_1^*(r', m, f)> = \int_{-T}^T e^{-i\pi\tau f} B(r, r', \xi, \tau) T\left(1 + \frac{\tau}{T}\right) d\tau$$
 (A.18)

but since the right hand side is the spectrum of the original POD kernel this suggests an estimator for the POD kernel of the form,

$$W_{1,1}^{T}(r,r',m,f) = \frac{\langle \hat{u}_{1}(r,m,f)\hat{u}_{1}^{*}(r',m,f) \rangle}{T}$$
$$= \int_{-T/2}^{+T/2} \left[1 - \frac{\tau}{T}\right] B(r,r',\xi,\tau) e^{(-i2\pi f\tau)} d\tau \qquad (A.19)$$

Equation A.19 provides an estimator of the POD kernel given in A.1. This representation was utilized in a numerical solution of the POD integral eigenvalue equation. The spectral estimator was calculated using many integral scale time blocks so that the lag window did not influence the results (Tan-atichat and George, 1985). The numerical implementation of the kernel estimator is discussed in chapter 6.

Appendix B

Orthogonal Eigenfunction Proof

The POD eigenfunctions are orthogonal over the rdr plane by the following proof. The equation defining the eigenfunctions is the integral eigenvalue equation of section 2.4,

$$\int W_{i,j}(r,r',m,f)\phi_j^n(r',m,f)r'dr' = \lambda^n(m,f)\phi_i^n(r,m,f)(n=1,2,3,\ldots)$$
 (B.1)

Both sides of eq. B.1 are multiplied by the conjugate eigenfunction $\phi_i^{p*}(r, m, f)$ and the weighting function rdr which produces,

$$\int \int W_{i,j}(r,r',m,f)\phi_{j}^{n}(r',m,f)\phi_{i}^{p*}(r,m,f)r'dr'rdr = \lambda^{n}(m,f)\int \phi_{i}^{n}(r,m,f)\phi_{i}^{p*}(r,m,f)rdr$$
(B.2)

Using the Hermitian nature of the kernel, $W_{i,j}(r,r') = W_{j,i}^*(r',r)$, yields,

$$\int \left\{ \int W_{j,i}(r,r',m,f) \phi_i^{p*}(r,m,f) r dr \right\} \phi_j^n(r',m,f) r' dr' =$$

$$\lambda^n(m,f) \int \phi_i^n(r,m,f) \phi_i^{p*}(r,m,f) r dr \tag{B.3}$$

but the term in curly brackets is the left hand side of eq. B.1 which when replaced by the term on the right hand side becomes,

$$\int \lambda^{p}(m,f)\phi_{j}^{p*}(r',m,f)\phi_{j}^{n}(r',m,f)r'dr' = \lambda^{n}(m,f)\int \phi_{i}^{n}(r,m,f)\phi_{i}^{p*}(r,m,f)rdr$$
(B.4)

which becomes,

$$(\lambda^{p}(m,f) - \lambda^{n}(m,f)) \int \phi_{j}^{p*}(r,m,f)\phi_{j}^{n}(r,m,f)rdr$$
(B.5)

or more succinctly,

$$\int \phi_j^{p*}(r, m, f) \phi_j^n(r, m, f) r dr = \begin{cases} \kappa & \text{if } \lambda^p = \lambda^n \\ 0 & \text{if } \lambda^p \neq \lambda^n \end{cases}$$
(B.6)

So the eigenfunctions are orthogonal on an r weighted basis.